Numerical simulation of growth of silicon germanium single crystals

by

Mandeep Sekhon
B.Tech, Punjab Technical University, 2005
M.Tech, Indian Institute of Technology Delhi, 2008

A Dissertation Submitted in Partial Fulfillment
of the Requirements for the Degree of

DOCTOR OF PHILOSOPHY

in the Department of Mechanical Engineering

©Mandeep Sekhon, 2015
University of Victoria

All rights reserved. This thesis may not be reproduced in whole or in part,
by photocopy or other means, without the permission of the author.

Supervisory Committee

Numerical simulation of growth of silicon germanium single crystals

by

Mandeep Sekhon
B.Tech, Punjab Technical University, 2005
M.Tech, Indian Institute of Technology Delhi, 2008

Supervisory Committee

Dr. Sadik Dost, Supervisor
(Department of Mechanical Engineering)

Dr. Ben Nadler, Departmental Member
(Department of Mechanical Engineering)

Dr. Peter Oshkai, Departmental Member
(Department of Mechanical Engineering)

Dr. Alexandre G. Brolo, Outside Member
(Department of Chemistry)

Abstract

Supervisory Committee

Dr. Sadik Dost, Supervisor
(Department of Mechanical Engineering)

Dr. Ben Nadler, Departmental Member
(Department of Mechanical Engineering)

Dr. Peter Oshkai, Departmental Member
(Department of Mechanical Engineering)

Dr. Alexandre G. Brolo, Outside Member
(Department of Chemistry)

Si_xGe_{1-x} is a promising alloy semiconductor material that is gaining importance in the semiconductor industry primarily due to the fact that silicon and germanium form a binary isomorphous system and hence its properties can be adapted to suit the needs of a particular application. Liquid phase diffusion (LPD) is a solution growth technique which has been successfully used to grow single crystals of Si_xGe_{1-x}. The first part of this thesis discusses the development of a fixed grid solver to simulate the LPD growth under zero gravity condition. Initial melting is modeled in order to compute the shape of the initial growth interface along with temperature and concentration distribution. This information is then used by the solidification solver which in turn predicts the onset of solidification, evolution of the growth interface, and temperature and concentration fields as the solidification proceeds. The results are compared with the previous numerical study conducted using the dynamic grid approach as well as with the earth based experimental results. The predicted results are found to be in good qualitative agreement although certain noticeable differences are also observed owing to the absence of convective effects in the fixed grid model. The second part investigates the effects of crucible translation on the LPD technique using the dynamic grid approach. The case of constant pulling is examined first and compared with the available experimental results. Then a dynamic pulling profile obtained as a part of simulation process is used to achieve the goal of nearly uniform composition crystal. The effect of crucible translation on the interface shape, growth rate, and on the transport process is investigated. Finally, the effect of magnetic field on the LPD growth is examined.

Contents

List of Tables vii

List of Figures viii

Acknowledgments xv

Dedication xvi

1 Introduction 1

1.1 Motivation and Goals 1

1.1.1 To develop a fixed grid numerical simulation methodology for single crystal growth of Si_xGe_{1-x} using the LPD growth technique under zero gravity condition 2

1.1.2 To numerically investigate the effects of crucible translation in the LPD growth of Si_xGe_{1-x} 3

1.1.3 To numerically simulate the LPD growth technique under the combined influence of crucible translation and static magnetic field 4

1.1.4 To numerically examine the effects of rotating magnetic field on the LPD growth technique 5

1.2 Thesis structure 6

2 Fundamentals 7

2.1 Relevant material science preliminaries 7

2.1.1 Unit cell representation of crystal structure 7

2.1.2 Crystallographic points, directions and planes 8

2.1.2.1 Crystallographic points 9

2.1.2.2 Crystallographic direction 9

2.1.2.3 Crystallographic planes 9

2.1.3 Close packed representation of crystal structure 10

2.1.4 Defects in crystalline solids 10

2.1.4.1 Point defects 10
2.1.4.2 Linear defects 11
2.1.4.3 Two dimensional defects 12
2.1.5 Solid solution 13
2.1.6 Phase diagram 14
2.1.7 Electrical properties of solids 15
2.1.7.1 Band structure 15
2.1.7.2 Drift velocity 16
2.1.8 Semiconductors 17
2.1.8.1 Intrinsic semiconductors 17
2.1.8.2 Extrinsic semiconductors 17
2.1.9 Silicon and Germanium 19
2.2 Single crystal growth techniques 20
2.3 Issues with established melt growth techniques for growing Si_xGe_{1-x} 24
2.4 Liquid Phase Diffusion growth technique 25
2.5 OpenFOAM and Finite Volume Discretization 29
2.5.1 Convection term 30
2.5.2 Diffusion Term 31
2.5.3 Source Term 32
2.5.4 Temporal Discretization 32
2.5.5 Solution of system of linear algebraic equations 33

3 Numerical simulation of the LPD growth technique using a fixed grid approach 34
3.1 Introduction 34
3.2 Model description 35
3.2.1 Modeling the melting process of germanium 35
3.2.2 Modeling the solidification of Si_xGe_{1-x} 36
3.2.3 Choice of the CFD solver 36
3.2.4 Numerical solution domain 37
3.2.5 Field equations 37
3.2.5.1 Melting Process 37
3.2.5.2 Solidification Process 39
3.2.5.3 Quartz wall and solid source 40
3.2.6 Solution algorithm 40
3.2.6.1 Melting solver 40
3.2.6.2 Solidification solver 41
3.2.7 Numerical Solution 42
3.2.7.1 Boundary and Initial condition 42
3.3 Results and Discussion 43

3.4 Inclusion of convective effects . . . 49
3.5 Summary . . . 49

4 Numerical investigation of the effects of crucible translation in the LPD growth of Si_xGe_{1-x} 50
4.1 Introduction . . . 50
4.2 Numerical Simulation . . . 51
4.2.1 Choice of the CFD solver . . . 51
4.2.2 Numerical solution . . . 52
4.2.3 Assumptions . . . 52
4.2.4 Field equations in the presence of moving boundary . . 53
4.2.4.1 Liquid Phase . . . 54
4.2.4.2 Solid Phase . . . 55
4.2.5 Computational aspects related to moving grid approach 55
4.2.5.1 Space conservation law . . . 55
4.2.6 Boundary conditions . . . 56
4.2.6.1 Concentration Field . . . 56
4.2.6.2 Thermal field . . . 57
4.2.6.3 Flow field . . . 58
4.3 Results and Discussion . . . 58
4.4 Summary . . . 67

5 Numerical simulation of the LPD growth technique subjected to magnetic field 69
5.1 Static magnetic field . . . 69
5.1.1 Introduction . . . 69
5.1.2 Assumptions . . . 70
5.1.3 Field equations in the presence of static magnetic field 70
5.1.4 Results and discussion . . . 70
5.2 Rotating magnetic field . . . 74
5.2.1 Introduction . . . 74
5.2.2 Assumptions . . . 75
5.2.3 Field equations in the presence of rotating magnetic field 75
5.2.4 Results and discussion . . . 77
5.3 Summary . . . 77

6 Conclusion 79
6.1 Contributions . . . 79
6.2 Future work . . . 81

Bibliography 82

List of Tables

3.1 Thermophysical properties of SiGe system 40
3.2 Comparison of growth thickness and interface evolution . . . 44

4.1 Coefficients used to compute equilibrium composition 57

List of Figures

2.1 Various types of unit cells . . . 8
2.2 Crystallographic a) points b) vector c) plane . . . 9
2.3 Close pack representation of crystal structure . . . 10
2.4 Various types of point defects . . . 11
2.5 Linear defects . . . 12
2.6 Two dimensional defects . . . 13
2.7 Illustration of the information conveyed by a binary phase diagram . . . 15
2.8 Band diagram . . . 16
2.9 Atomic bonding in an intrinsic semiconductor . . . 18
2.10 Extrinsic semiconductor (n type) . . . 19
2.11 Extrinsic semiconductor (p type) . . . 20
2.12 Phase diagram of silicon germanium . . . 21
2.13 Schematic diagram of Czochralski crystal growth . . . 22
2.14 Schematic diagram of Vertical Bridgman and its temperature profile . . . 23
2.15 Schematic diagram of LPD growth technique (left half domain shown) and its temperature profile . . . 24
2.16 Schematic diagram of THM and its temperature profile . . . 25
2.17 Illustration of LPD growth technique . . . 28

3.1 Simulated crystal growth . . . 45
3.2 Computed isotherms and isoconcentration lines . . . 46
3.3 Comparison of the evolution of interface with previous numerical and experimental results . . . 46
3.4 Computed Radial and axial composition profiles . . . 47
3.5 Experimentally measured radial and axial composition profiles 47
3.6 Variation of average growth velocity with time . . . 48

4.1 Experimental centreline composition profiles of the translated (at 0.429mm/h) and stationary (at 0 mm/h) LPD . . . 59

4.2 Experimental radial composition profiles of the translated (at 0.429mm/h) and stationary (at 0 mm/h) LPD 59
4.3 Computed axial silicon composition profiles along the centreline of the crystal at a translation rate of 0 mm/hr (stationary), at a constant rate of 0.429 mm/h, and using a dynamic translation (pulling) profile 60
4.4 Computed radial silicon composition profiles of the crystal at a translation rate of 0 mm/hr (stationary), at a constant rate of 0.429 mm/h, and using a dynamic translation (pulling) profile 60
4.5 Computed average interface temperature at a translation rate of 0 mm/hr (stationary), at a constant rate of 0.429 mm/h, and using a dynamic translation (pulling)profile 61
4.6 Dynamic translation (pulling) profile used in the numerical simulation 61
4.7 Computed interface evolution for a growth period of 20 hours at various translation rates 62
4.8 Velocity magnitude in the melt at various simulation times with no translation 62
4.9 Velocity magnitude in the melt at various simulation times with a translation rate of 0.429 mm/h 63
4.10 Velocity magnitude in the melt at various simulation times with a dynamic translation 63
4.11 Thermal field in the complete domain at various simulation times with no translation 64
4.12 Thermal field in the complete domain at various simulation times with a translation rate of 0.429 mm/h 64
4.13 Thermal field in the complete domain at various simulation times with dynamic translation 65
4.14 Concentration field in the melt at various simulation times with no translation 65
4.15 Concentration field in the melt at various simulation times with a translation rate of 0.429 mm/h 66
4.16 Concentration field in the melt at various simulation times with dynamic translation 66

5.1 Velocity magnitude in the melt during early hours of growth . 71
5.2 Velocity magnitude in the melt during early hours of growth under the action of applied static magnetic field of 0.4 T . . . 72
5.3 Comparison of interface evolution for a growth period of 36 hours without and with static magnetic field 72

5.4 Computed axial silicon composition profiles along the centre-line of the crystal under the action of applied static magnetic field of 0.4 T at a translation rate of 0 mm/hr (stationary) and using a dynamic translation (pulling) profile 73
5.5 Dynamic translation (pulling) profile for producing low silicon composition (1.1 % atm) crystal under the action of applied static magnetic field of 0.4 T 73
5.6 Comparison of interface displacement after growth period of 5.5 hours and applied static magnetic field of 0.4 T without and with dynamic translation 74
5.7 Simulation results after 1 hr of growth time in the presence of RMF 77
5.8 Computed axial composition profile with and without RMF . 78

Nomenclature

Roman Symbols

$\mathbf{a}$	General vector
A	Coefficient matrix
a	Matrix coefficient
$\mathbf{B}$	Magnetic field
B	Magnetic field amplitude
C	Concentration
c_p	Specific heat
Co	Courant number
$\mathbf{d}$	Vector joining cell centres
D	Mass diffusivity
d	Translated distance
e	Charge on electron
$\mathbf{F}$	Lorentz force
F	Fluid flow flux
F_s	Mesh motion flux
H	Enthalpy
K	Partition coefficient

L	Latent heat
$\mathbf{n}$	Unit vector normal to the surface
n	Number of free electrons per unit volume
n_e	Free electron concentration in an extrinsic semiconductor
n_i	Intrinsic carrier concentration
P	Pressure
p	Pull Rate
p_e	Hole concentration in an extrinsic semiconductor
R	Source vector
r	Radial coordinate
$\mathbf{S}$	Surface normal area vector
S	Surface area
S_ϕ	Source term
S_C	Sink term in mass transport equation
S_E	Explicit part of source term
S_I	Implicit part of source term
S_T	Sink term in energy equation for melting
$S_T^{'}$	Source term in energy equation for solidification
t	time
T	Temperature
T_{max}	Maximum temperature at the top of outer crucible wall
$\mathbf{U}$	Fluid velocity
$\mathbf{U_g}$	Grid velocity
$\mathbf{v}$	Drift velocity

V	Volume
A	Vector of unknowns at cell centres
y	Distance between face centre and origin
z	Axial coordinate

Greek Symbols

α	Thermal diffusivity
β	Emissivity
β_C	Solutal volumetric expansion coefficient
β_T	Thermal volumetric expansion coefficient
Δt	Time step
$\Delta\gamma$	Actual mass fraction solidified in a given cell in a single time step
$\Delta\gamma_{lever}$	Mass fraction solidified in a given cell in a single time step as per lever rule
ϵ	Liquid fraction
Γ	Transport property
γ	Cumulative sum of mass fraction solidified in a given cell
λ	Thermal conductivity
μ	Dynamic viscosity
μ_e	Electron mobility
μ_h	Hole mobility
ω	Angular frequency
ϕ	General scalar transport variable
ρ	Density
σ	Electrical conductivity
$\varPhi$	Scalar potential

φ Tangential direction

Superscripts

dis Dissolution interface

eq Equilibrium

$growth$ Growth interface

N Number of time steps after solidification starts in a given cell

n Current time step

$n-1$ Previous time step

N_T Total number of time steps in which a cell completely solidifies after it is captured as a solidifying cell

rot Rotating magnetic field contribution

Subscripts

amb Ambient

f Variable value at face centre

l Liquid phase

max Maximum

N Variable value at neighbouring cell centre

P Variable value at cell centre

r Radial direction

ref Reference

s Solid phase

z Axial direction

Acknowledgments

I would like to express my sincere gratitude to Dr. Sadik Dost for picking my grad school application and letting me live my Ph.D dream. I really appreciate the guidance, financial support, and the creative freedom he offered me to pursue my own ideas. His support and advice during the paper writing helped a lot. I am equally appreciative of the guidance of Mr. Brian Lent who was always more than willing to help in every possible way and share his vast knowledge in the field of crystal growth. The task of correcting the thesis became a lot easier because of his help. I am really thankful to my senior colleagues Dr. Neil Armour for his insightful comments about my research work and Mr. Jordan Roszmann for always helping me out whenever I got stuck. The Ph.D theses of Dr. Neil Armour and Dr. Mehmet Yildiz were instrumental in getting me started and developing an understanding of this research topic.

I am grateful to Dr. Ben Nadler, Dr. Peter Oshkai, and Dr. Alexandre G. Brolo for agreeing to serve on my supervisory committee. A couple of thanks are also due back home to some special people including Dr. S.C. Mullick (Professor emeritus, I.I.T Dehi), Dr. T.C. Kandpal (Professor, I.I.T Dehi) and Mr. G. Viswanathan (former G.M. , B.H.E.L Trichy) who all have had a very deep influence on me and some of my close friends Lalit, Rajeev, and Durai from whom I have learnt a lot. Last but by no means the least I need to thank my parents and my brother for their unconditional love and support.

Dedication

To the Almighty for always "being there"
To Mummy, Papa, and my brother for their love.

Chapter 1

Introduction

1.1 Motivation and Goals

The interest in alloy semiconductor material Si_xGe_{1-x} stems primarily from the fact that it forms a binary isomorphous system indicating complete solid and liquid state miscibility. From an application's perspective, this means that by selecting an appropriate alloying ratio it can meet the requirements of a diverse set of applications. It is useful both in epitaxial and bulk crystal form. However, an inherent difficulty with this alloy system is the wide gap between solidus and liquidus lines in its phase diagram. The large difference in the melting points of silicon and germanium makes the solidus and liquidus lines extremely temperature sensitive and any temperature variation during the melt growth of the bulk crystals of this material can lead to significant compositional variation [1]. Moreover, the solid state solubility of silicon in germanium is greater than the liquid state solubility, which means silicon moves from the melt to the solidifying crystal across the interface, thereby depleting the melt of silicon as growth proceeds and thus the melt needs to be fed with silicon in order to obtain uniform composition crystal [1]. Due to these difficulties in using the melt growth techniques to grow uniform composition bulk Si_xGe_{1-x}, there is a need to look into other growth techniques. One such technique is the liquid phase diffusion (LPD) growth, originally developed in reference [2] as a variant of the multicomponent zone melting technique. This technique belongs to the family of solution growth techniques and works on the principle of saturation and precipitation. It has been successfully used to produce graded composition Si_xGe_{1-x} single crystals [3] and its numerical analysis is the subject of this thesis.

Numerical simulations play a crucial role in developing deeper understand-

ing of various physical processes occurring during crystal growth. The insights gained with numerical studies can help in better design of experiments and can ultimately lead to better quality of grown crystals. It can be immensely useful in bringing down the costs associated with experimentation as it reduces the dependence on the trial and error approach often resorted to, in most experimental work. Further, it can significantly speed up the process development cycle. With the advent of modern computers and enormous amount of computing power available even on an ordinary desktop, the reliance on computational approach to solve complex engineering and science problems is on the rise. However, this approach comes with its own set of limitations and obtaining reliable results can still be quite challenging. From a numerical modeling perspective, one of the major issues associated with simulating crystal growth is that of the moving boundary. The first part of this thesis addresses this problem by developing a computationally efficient and accurate simulation methodology based on a fixed grid approach to simulate the LPD growth method under zero gravity condition. The second major thrust area of this research work is to numerically determine the crystal pulling profile to grow nearly uniform composition Si_xGe_{1-x} crystals unlike its original version which produces graded composition crystals. Finally, the effect of magnetic field on the LPD growth is explored numerically. Specific aims and objectives of this study along with the relevant previous work are discussed next.

1.1.1 To develop a fixed grid numerical simulation methodology for single crystal growth of Si_xGe_{1-x} using the LPD growth technique under zero gravity condition

- **Previous work**- The fixed grid approach is one of the most widely used computational techniques for solidification/melting problems. The enthalpy-porosity technique [4] is based on the fixed grid approach and has been successfully used to simulate various melt growth techniques [5–9] . However, the conventional enthalpy method cannot be used to model solidification in the LPD growth because it is a solution growth technique in which solidification is driven by saturation and precipitation unlike melt growth technique where solidification is achieved by cooling the melt below its liquidus temperature. A numerical model was developed in reference [10] for the LPD process based on continuum theory. A moving grid approach was employed to carry out the numerical simulation and the results were presented in terms of evolution of

the growth interface shape and temperature, concentration, and flow fields in the melt. Further, the suitability of using the smoothed particle hydrodynamics numerical technique to simulate the LPD process was explored in references [11, 12] .

- **Specific objectives**
  - Develop a fixed grid numerical solution methodology to simulate the complete LPD process under zero gravity condition.
  - Obtain useful information from simulation results such as crystal composition in radial and axial direction.
  - Compare the simulation results with the previous numerical (carried out using a moving grid approach) and experimental work.
- **Significance**
  - The developed numerical procedure can be used to obtain the numerical solution for the LPD technique in a relatively simple and quick way, avoiding the complexities of a moving grid approach such as the need to create a boundary conforming mesh.
  - The fixed grid approach allows for longer simulation time thereby allowing the simulation of the complete crystal growth process.

1.1.2 To numerically investigate the effects of crucible translation in the LPD growth of Si_xGe_{1-x}

- **Previous work**- In order to produce compositionally uniform crystals in the LPD growth technique, the interface should be maintained at a constant temperature during growth. This can be accomplished by translating the sample at a speed synchronized with the growth rate. Originally, the LPD technique was developed as a variant of multicomponent zone melting and sample translation rate was determined empirically [2]. In reference [13], an in situ monitoring system was developed and used to observe and control the temperature of the crystal-melt interface. This arrangement was used to study the effect of constant translation rate which was determined by monitoring the growth rate with no sample translation. Subsequently, in reference [14], a feedback control system was developed to keep the interface at a fixed position with the objective of growing uniform composition crystals and pull rate was corrected dynamically in order to maintain constant interface temperature thereby addressing the needs of a situation in which

growth does not become constant but varies dynamically. Experimental investigation of the effect of constant translation rate on the LPD growth was conducted in reference [15]. A complete melt back of seed was observed due to disturbance in the thermal conditions caused by the inclusion of a translation mechanism in the system and led to polycrystalline growth but relatively flatter axial composition profiles were obtained after an initial graded region in comparison to the case of no translation [15].

- **Specific objectives**
  - Numerically study the effect of crucible translation on crystal composition, average interface temperature, and its shape.
  - Study the role of natural convection under crucible translation condition.
  - Determine the dynamic pulling profile which can result in nearly uniform crystal composition.
  - Effect of crucible translation on growth rate.
- **Significance**
  - The numerical results can help in better design of LPD experiments with crucible translation by giving useful information to the experimentalist such as optimum pull rate, pull initiation time and total growth time. The dynamic pulling profile thus obtained can be used in experiments to grow nearly uniform composition crystals.

1.1.3 To numerically simulate the LPD growth technique under the combined influence of crucible translation and static magnetic field

- **Previous work**-Static magnetic field is used in semiconductor crystal growth applications for suppressing natural convection and hence improving the quality of the grown crystals [16, 17]. Numerical examination of the effects of static magnetic field on an earth based LPD growth system was carried out in references [18, 19] and it was found that static field was effective in suppressing the natural convection but did not alter the growth interface shape significantly. This was followed by experimental work [20], in which magnetic field effects were examined experimentally and it was observed that the application of

a static magnetic field reduced the mass transport of silicon due to altered thermal field and also due to suppression of natural convection.

- **Specific objectives**
  - Time evolution of the growth interface for the LPD process subjected to static magnetic field and crucible translation.
  - Effect of the combination of crucible translation and static magnetic field on the transport process, crystal composition, and growth rate.
- **Significance**
  - Usage of static magnetic field can suppress the natural convection and can be helpful in growing uniform composition crystals of low silicon concentration by allowing the dynamic crucible pulling to be initiated during the early hours of growth.

1.1.4 To numerically examine the effects of rotating magnetic field on the LPD growth technique

- **Previous work**-Rotating magnetic field (RMF) is routinely used in the material processing industry for stirring application [21]. In the area of crystal growth, the usage of RMF improves the uniformity of thermal and concentration fields without introducing any mechanical contact and on a practical level it is much easier to implement than the static magnetic field [22]. Numerical examination of the effects of RMF on an earth based LPD growth system was carried out in references [18, 19]. RMF was found to be effective in flattening the growth interface shape. Experimental investigation of these effects was carried out in reference [23] and it was shown that application of RMF significantly enhanced the silicon transport.
- **Specific objectives**
  - Effect of RMF on the distribution of thermal and concentration fields.
  - Influence of RMF on the growth rate.
- **Significance**
  - Application of RMF can speed up the growth process in the LPD technique to produce graded composition crystals from which the seed crystals of appropriate composition can be extracted.

1.2 Thesis structure

This work uses numerical simulation on a continuum scale as a tool to address a crystal growth problem. Accordingly, chapter 2 starts off by giving some grounding on the material science basics pertinent to this study. The discussion has been kept brief and the reader is referred to appropriate references for further details. Finite volume discretization is described next as this technique is used both in OpenFOAM and Ansys Fluent which have been used to carry out the numerical simulation. Chapter 3 discusses in detail, the simulation methodology developed to simulate the LPD process under zero gravity condition using a fixed grid approach. Modeling procedure for both melting and solidification are discussed at length. The results obtained using a fixed grid approach are compared with the previously obtained numerical results using a moving grid approach as well as with the experimental results. The next chapter delves into the investigation of the effects of crucible translation on the LPD technique. First, the effect of constant pull rate is examined followed by the investigation of dynamic pulling profile. Results are presented next in terms of radial, axial compositional plots, interface evolution plot as well as concentration, thermal and flow fields. The effect of static and rotating magnetic fields on the LPD growth method is examined next in chapter 5. Finally, chapter 6 summarizes the thesis, highlighting the key contributions of this work and closes by giving some pointers for the future work.

Chapter 2

Fundamentals

2.1 Relevant material science preliminaries

Material science basics related to crystal growth are discussed briefly. This section largely follows the text [24] and the reader is referred to it for further details.

2.1.1 Unit cell representation of crystal structure

Solid materials may be broadly grouped into two categories namely crystalline and amorphous. This classification is done on the basis of the regularity displayed in their atomic arrangement. Crystalline solids exhibit an orderly atomic arrangement whereas in amorphous solids such an order is absent. The actual spatial arrangement of atoms is known as the crystal structure and it influences the properties of that material. Crystal structure can be considered to be made up of a small repetitive entity called the unit cell. In connection with the crystal structure two other commonly used terms are the coordination number and the atomic packing factor. Coordination number indicates the number of nearest neighbouring atoms. Atomic packing factor as the name says, describes how closely the atoms are packed in a given unit cell. It is defined as the volume of the atoms in a unit cell per unit volume of that unit cell. Following are the commonly found crystal structures in most metallic materials:

1. Face centred cubic (FCC)- The unit cell for this crystal structure is cubical in shape and has atoms at the corners and also at the face centres. The corner atom is shared by eight unit cells and the face

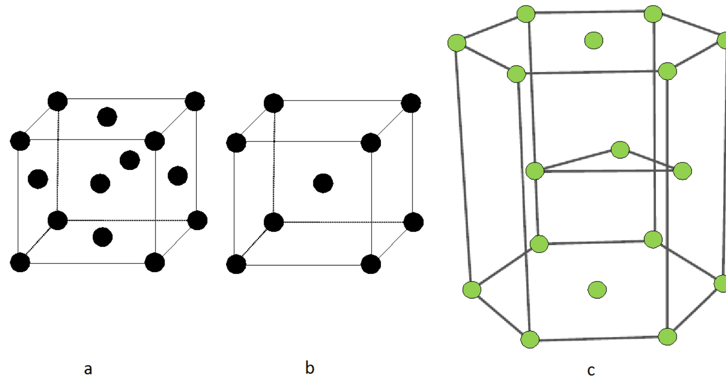

Figure 2.1: Various types of unit cells a) FCC b) BCC c) HCP

centre atom is shared amongst two unit cells. Thus the effective number of atoms per unit cell is four (8 X 1/8 + 6 X1/2). Copper, silver, and gold are some of the common examples of the FCC crystal structure.

2. Body centred cubic (BCC)- In this case the atoms are located at the eight corners of the unit cell and one at the centre of the cube. Thus the effective number of atoms per unit cell is two ((8 X 1/8 +1). Iron (α), tungsten, and chromium display the BCC crystal structure.

3. Hexagonal closed packed (HCP)- As the name says, its unit cell is hexagonal in shape. The top and bottom face which are regular hexagons, have atoms located at the corner and at the centre. In addition there are three atoms in the mid-plane. The effective number of atoms per unit cell in this case is six (12 X 1/6 + 2 X 1/2 + 3). Materials exhibiting this kind of crystal structure include cadmium, magnesium, and zinc.

The various types of unit cell discussed above are shown in figure 2.1. Crystal systems can be also be classified on the basis of geometry of the unit cell. The geometrical parameters of the unit cell which include the edge lengths and inter-axial angles are termed as lattice parameters. For instance, a cubic crystal system has all the three edges of equal length and all three inter-axial angles as 90°.

2.1.2 Crystallographic points, directions and planes

In order to refer to a point, direction or a plane within a unit cell standard rules have been developed which are discussed briefly below for the cubic crystal system and are shown in figure 2.2.

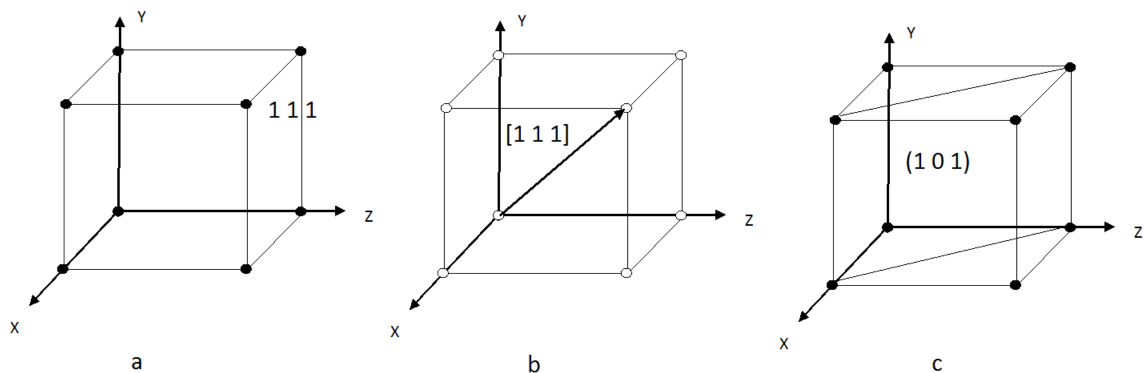

Figure 2.2: Crystallographic a) points b) vector c) plane

2.1.2.1 Crystallographic points

The position of a point within a unit cell is expressed in terms of coordinates which are the fraction of total length of the edge in that direction.

2.1.2.2 Crystallographic direction

It is specified by a vector joining the origin and a point in the unit cell. The length of the projection of this vector along three axes is expressed in terms of edge lengths in the three directions. The resulting three numbers are reduced to the smallest possible set of integers and enclosed in square brackets. Negative direction is indicated by an over-bar.

2.1.2.3 Crystallographic planes

A set of three numbers enclosed in parentheses known as the Miller indices is used to represent a crystallographic plane. When calculating the Miller indices for a plane it should be ensured that it does not pass through the origin, if it does then either the origin is shifted or another plane parallel to the original plane should be considered. The reciprocal of the intercepts of the plane along the three axes reduced to the smallest set of integers determines the Miller indices for that plane. Similar to the crystallographic directions negative intercepts are specified with the over-bar.

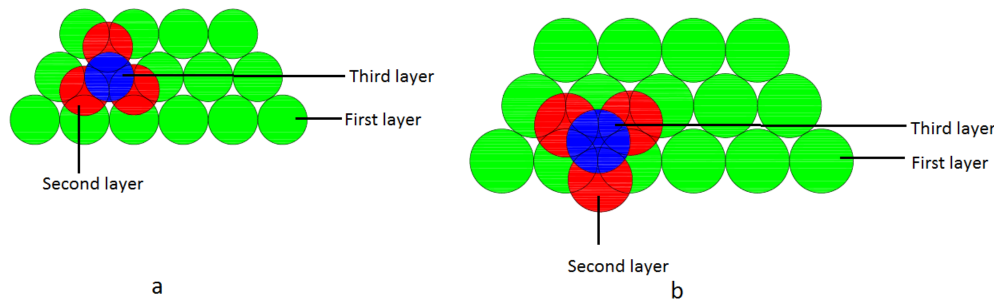

Figure 2.3: Close pack representation of crystal structure a) HCP b)FCC

2.1.3 Close packed representation of crystal structure

As can be seen in figure 2.3, another way of visualizing FCC and HCP crystal structures is to consider them to be made up of layers of close packed planes. To illustrate, consider a layer of close packed atoms which can be thought of as spheres. In this layer there are two kinds of triangular inter-sites, one with vertex pointing upwards and the other pointing downwards. The second layer of close packed atoms can be placed on either of the two. Placement of the third layer is what differentiates HCP from FCC. In the case of HCP, the third layer is placed such that the atoms of this layer lie exactly above the atoms of the first layer and is thus represented by ABAB... which indicates the piling arrangement of layers. However in the case of FCC, the third layer is placed in such a way that it covers the previously uncovered triangular inter-sites of the first layer and hence is represented by piling sequence of ABCABC... .

2.1.4 Defects in crystalline solids

Deviation from the idealized crystal structure is termed as crystal defect. This deviation can occur in a number of different ways and accordingly there are different crystal defects which are briefly discussed below and are illustrated in figure 2.4 :

2.1.4.1 Point defects

- Vacancies and self interstitial- If an atom is missing from its regular position in the lattice then it is called a vacancy. A self interstitial is

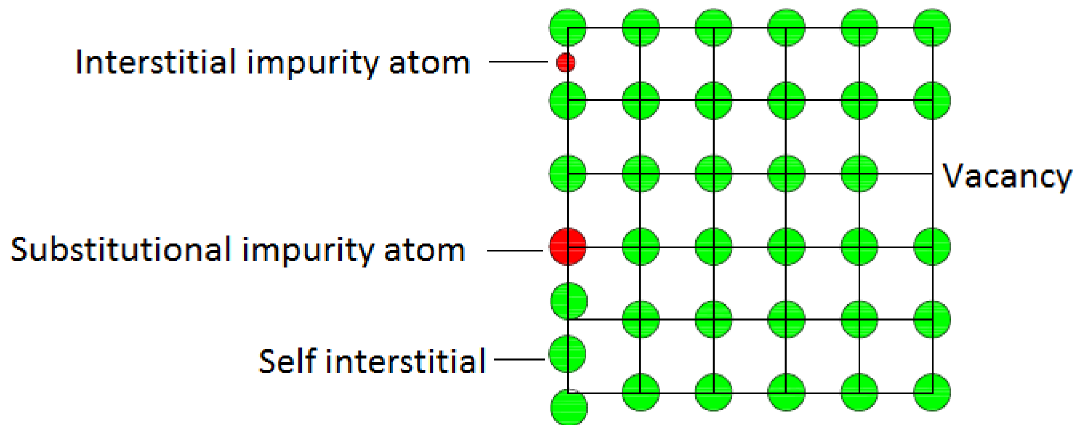

Figure 2.4: Various types of point defects

created if an atom instead of occupying its regular position is found at an inter-site created due to the close packed arrangement of atoms.

- Impurities- This represents the presence of foreign atoms in the crystal structure. When the crystal structure of the parent material is retained upon the addition of the foreign material then a solid solution is formed. Depending upon the position occupied by these foreign atoms in the parent crystal lattice there can be two types of solid solutions:
  - Substitutional solid solution in which the solute atom replaces the solvent atom in the crystal lattice.
  - Interstitial solid solution in which the solute atom occupies the inter-site in the solvent crystal lattice.

2.1.4.2 Linear defects

Dislocation refers to the irregular arrangement of the atoms along a line in a crystal structure. It is of the following types: (see figure 2.5) :

- Edge dislocation-When an extra half plane of atoms is introduced into the lattice then it results in an edge dislocation and it introduces regional distortion in the crystal structure. It is denoted by the symbol $\perp$.

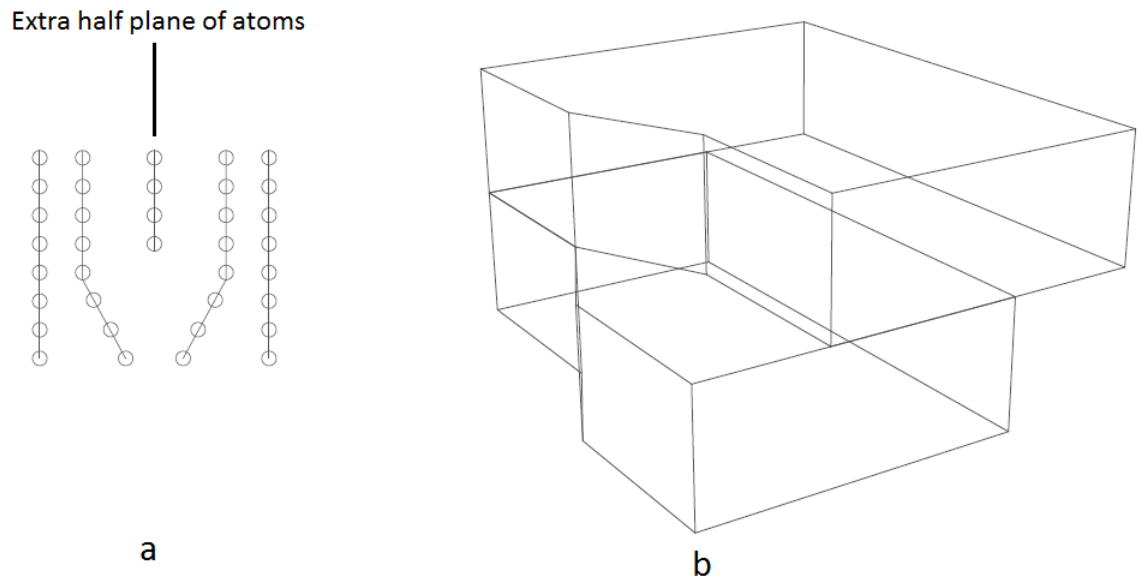

Figure 2.5: Linear defects a) Edge dislocation b) Screw dislocation

- Screw dislocation- This can be interpreted as a consequence of the application of shear stress to the crystal structure. As a result, misalignment occurs along a line due to relative motion between atomic planes. ↻ is used to represent the screw dislocation.
- Mixed dislocation- In actual crystalline solids, dislocations mostly occur as a combination of the edge and screw rather than being a pure edge or screw.

2.1.4.3 Two dimensional defects

These defects demarcate two different regions of the crystal structure. They are of the following types:

- External surfaces- As the name says, it represents the discontinuity of the crystal structure and the atoms lying in this region are at a higher state of energy compared to the atoms lying in the interior since the surface atoms are not bonded in all directions.
- Grain boundaries- These separate the regions of different crystallographic orientations (see figure 2.6 a).
- Twin boundaries- In this case a mirror image symmetry exists across the boundary (see figure 2.6 b).

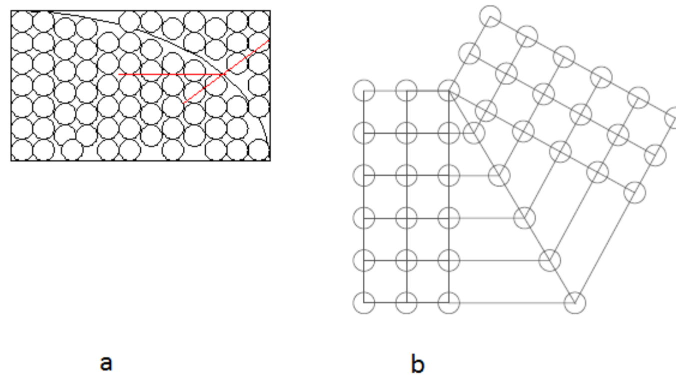

Figure 2.6: Two dimensional defects a) Grain boundary b) Twin boundary

- Stacking faults- As discussed earlier, the FCC crystal structure can be visualized with the help of layers of close packed planes. When there is deviation from this standard stacking sequence of atomic planes, it results in a stacking fault. For instance, the regular sequence of ABCABC... may be disrupted as ABABC... .

2.1.5 Solid solution

To understand the concept of solid solution we first need to understand the idea of phase. Phase is that region of a system under consideration which is characterized by distinct physical and/or chemical properties. For example, ice, water, and water vapour represent different phases since they have distinct physical properties even though their chemical composition is the same. Similarly every pure substance represents a different phase. When addition of one solid component to the other does not result in the formation of a new phase but the crystal structure of the parent material is retained then it is termed as solid solution. Whether two components would form a solid solution or not depends upon a number of factors such as their atomic radii, crystal structure etc . In connection with solutions, a commonly encountered term is the solubility limit which represents the maximum amount of solute that can be dissolved at a given temperature without the formation of an additional phase.

2.1.6 Phase diagram

These diagrams provide information about different equilibrium phases present at various combinations of temperature, pressure, and composition in a graphical form. Two of the commonly found phase diagrams are briefly discussed below:

- Unary-When there is only one component involved, then the phase diagram is said to be unary. These are basically pressure-temperature plots depicting various phases in which a pure substance can exist at various possible combinations of temperature and pressure.
- Binary- In this case there are two variables namely temperature and composition while pressure is held constant. Binary phase diagram provides the following information:
  - Number and type of phases present at a given temperature and composition.
  - Equilibrium composition of each phase- To determine the equilibrium composition of each phase at a given temperature, the intersection of the isotherm with the phase boundary is located and composition is then read corresponding to these intersection points (points A and C in figure 2.7).
  - Relative amounts of each phase- This is determined from the lever rule. Similar to the previous case, first an isotherm is drawn and the intersection with the phase boundaries is noted. The relative amount of a particular phase is obtained by dividing the composition difference between the other phase (whose relative amount is not being determined) and the given composition and the composition difference between the intersection points of the given isotherm and the phase boundaries. For instance to determine the composition of the solid phase in figure 2.7 , subtract the composition corresponding to A from B and divide it by the difference in the composition corresponding to C and A.

In the context of phase diagrams, a phase boundary above which there exists only liquid phase is called the liquidus line and below which there exists only solid phase is known as the solidus line.

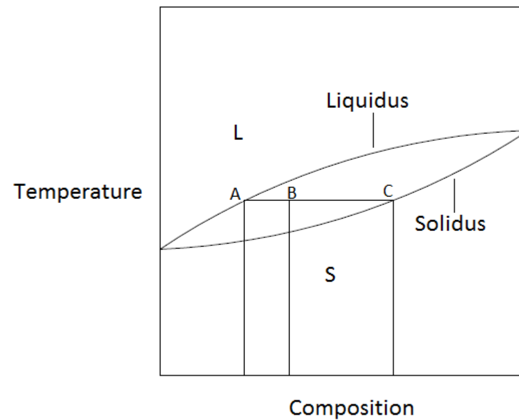

Figure 2.7: Illustration of the information conveyed by a binary phase diagram

2.1.7 Electrical properties of solids

Solid materials may be classified based on the response of the material when subjected to an external electrical field. Depending upon the material in question, there may be flow of electric current, limited flow or no flow at all. This behaviour is quantified by a property called the electrical conductivity. For conductors, conductivity is around 10^7 mho/m, for semiconductors its value lies in between 10^{-6} to 10^4 mho/m and for insulators it is in between 10^{-10} to 10^{-20} mho/m. This different behaviour can be explained on the basis of availability of free charge carriers responsible for the flow of current under the action of an applied electric field. The most common form of charge carriers are free electrons.

2.1.7.1 Band structure

For a single atom there exists a number of discrete energy levels corresponding to different shells and sub-shells. Electrons are filled in these shells and sub-shells in the ascending order of energy level represented by them. When millions of such atoms are brought together and are arranged in an orderly manner to form a crystalline solid, the discrete nature of the energy levels associated with a single atom is lost and it gives rise to continuous energy bands. At absolute zero, all the valence electrons are present in an energy band called the valence band. For a valence electron to participate in the conduction process, it must cross a threshold energy level barrier so that it is freed from the atom and can move in the lattice under the influence of an

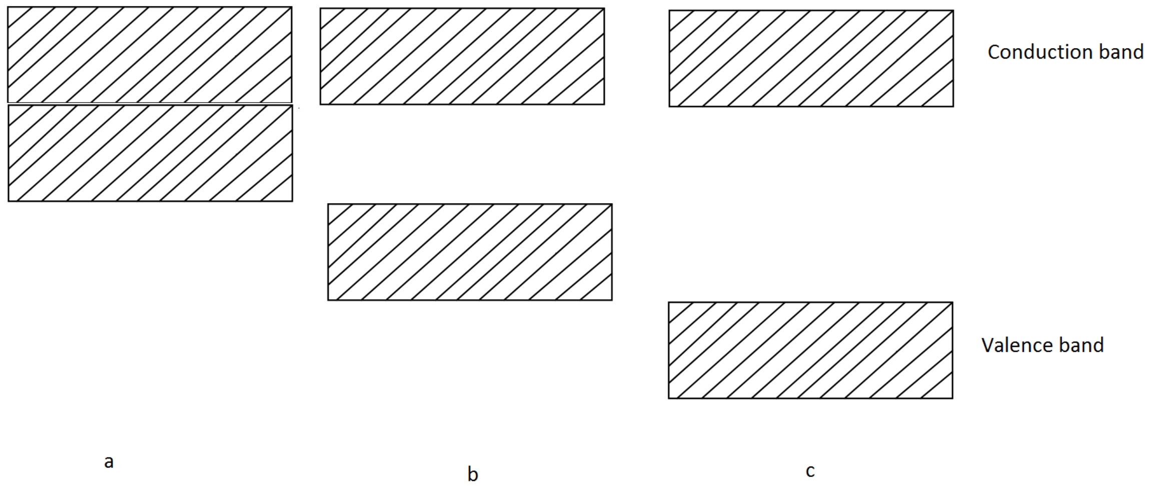

Figure 2.8: Band diagram a) Metals b) Semi conductors c) Insulators

applied electric field. When a valence electron is elevated to a energy level where it can participate in the conduction process, it is said to be in the conduction band. The difference between the highest energy level in the valence band and lowest energy level in the conduction band is called the band gap. There is no permissible energy level within the band-gap. For conductors, the valence band and the conduction band overlap, hence a large number of valence electrons get easily promoted to the conduction band which explains the flow of electric current under the action of an electric field. However, in insulators this band gap is too wide($>$2eV) which prevents the valence electrons from moving into the conduction band. Finally, in semiconductors, the band-gap is relatively narrow ($<$ 2eV) which is responsible for limited flow of current through these materials. The various types of band diagram are illustrated in figure 2.8.

2.1.7.2 Drift velocity

Under the action of an applied electric field, electrons in the conduction band accelerate but also experience resistance due to various crystal defects and atomic vibrations. However, there is net movement of electrons and the average velocity with which electrons move in the direction of the applied electric field is directly proportional to this field. It is given as follows:

$$\mathbf{v} = \mu_e \mathbf{E} \tag{2.1}$$

The electron mobility μ_e is the measure of the ease with which electrons flow in the lattice under the action of the applied electric field. The electrical conductivity is related to the mobility as follows:

$$\sigma = n|e|\mu_e \tag{2.2}$$

2.1.8 Semiconductors

As discussed previously, semiconductors represent a class of materials whose electrical conductivity lies in between that of conductors and insulators due to their band structure. The extreme sensitivity of their electrical properties on the presence of impurities makes them particularly attractive for a wide range of applications.

2.1.8.1 Intrinsic semiconductors

The electrical properties of intrinsic semiconductors are controlled by the charge carriers of the pure material and not the impurities. An important term used in the context of semiconductors is hole. When an electron is elevated to the conduction band from the valence band it leaves behind a vacancy in the valence band which is filled by a nearby electron. We can think of the motion of these valence electrons in terms of charge carriers called holes having the same charge as that of an electron but opposite in sign. Thus, under the action of an electric field the flow of electric current can be attributed to the motion of free electrons in the conduction band and motion of holes in the valence band. The electrical conductivity for intrinsic semiconductors is given as:

$$\sigma = n_i|e|(\mu_e + \mu_h) \tag{2.3}$$

For intrinsic semiconductors the number of free electrons is equal to the number of holes. Atomic bonding for intrinsic silicon is shown in figure 2.9.

2.1.8.2 Extrinsic semiconductors

In these materials, impurities are added intentionally so as to alter the material's electrical properties. Depending upon the nature of the impurity they can be of two types:

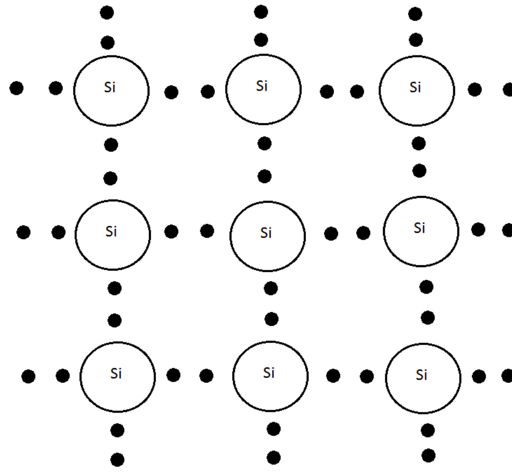

Figure 2.9: Atomic bonding in an intrinsic semiconductor

- n-type- In this type of semiconductors, the donor type of impurity is added. Donor atoms form a substitutional solid solution. Donor atoms contain excess valence electrons than required to form a covalent bond with other host atoms and this results in the creation of additional free electrons apart from the ones already present due to parent semiconductor material. In terms of band model, this can be viewed as creation of a new donor energy level very near to the conduction band thereby requiring very little energy to promote valence electrons belonging to donor atoms to the conduction band (see figure 2.10 b). The contribution of holes to the electrical conductivity is negligible in comparison to free electrons in this type of semiconductor. n type indicates the sign of the majority charge carriers which are electrons while holes are minority charge carriers in this case. Phosphorous, Arsenic, and Antimony are some of the examples of donor type of impurity for silicon.

$$\sigma \cong n_e|e|\mu_e \tag{2.4}$$

- p-type- In this case an acceptor type impurity is the doping material. The acceptor impurity atom forms a substitutional solid solution and contains fewer valence electrons than required to form the covalent bond with other host atoms leading to the creation of an excess hole in the valence band. As mentioned before, holes in the valence band also participate in the conduction process under the action of an applied electric field. This can also be viewed as a consequence of the creation of an additional acceptor energy level very close to the conduction band

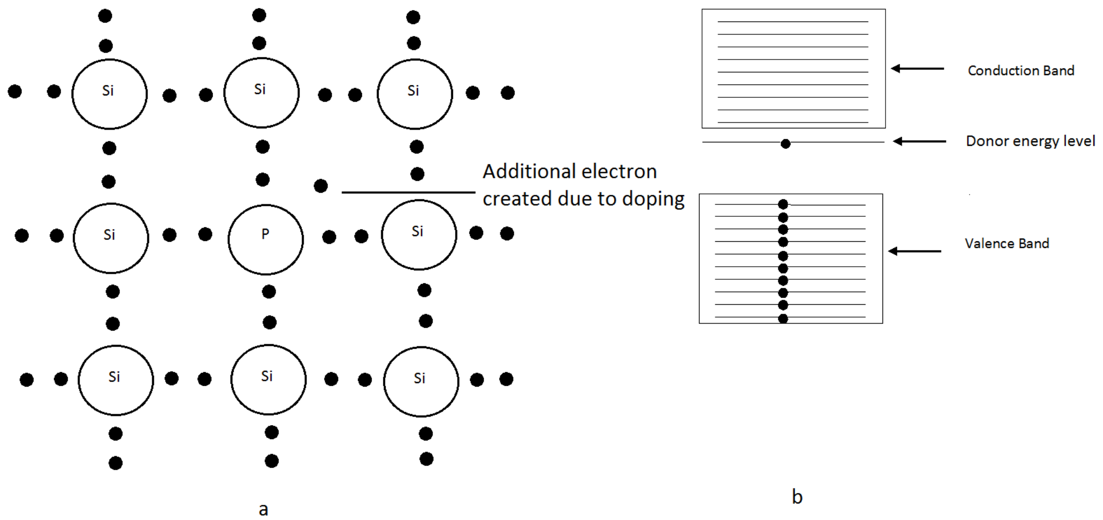

Figure 2.10: Extrinsic semiconductor (n type) a) Atomic bonding b) Band diagram

of the parent material (see figure 2.11b). As a result, valence electrons in the valence band get easily promoted to the newly created acceptor energy level leaving behind a hole in the valence band. These are the additional holes created apart from the ones created due to promotion of electrons from valence to conduction band. In this case holes are the majority charge carriers and hence the name p type.

$$\sigma \cong p_e|e|\mu_h \tag{2.5}$$

2.1.9 Silicon and Germanium

Silicon and germanium are the two most important semiconductor materials from an application's point of view. Silicon has an atomic number of 14 while that of germanium is 32. Both of them have 4 valence electrons and are consequently placed in group IVA of the periodic table. They crystallize with the diamond lattice structure. The phase diagram of silicon germanium belongs to the category of binary isomorphous system which means that they exhibit complete solid and liquid state miscibility. This is on expected lines as both have nearly the same atomic radii , similar crystal structure, and four valence electrons. The complete miscibility of silicon in germanium makes it useful for various applications as the alloying ratio can be chosen as per the requirement. Another noteworthy feature of this phase diagram is the wide gap between the solidus and the liquidus line. The band gap of silicon is

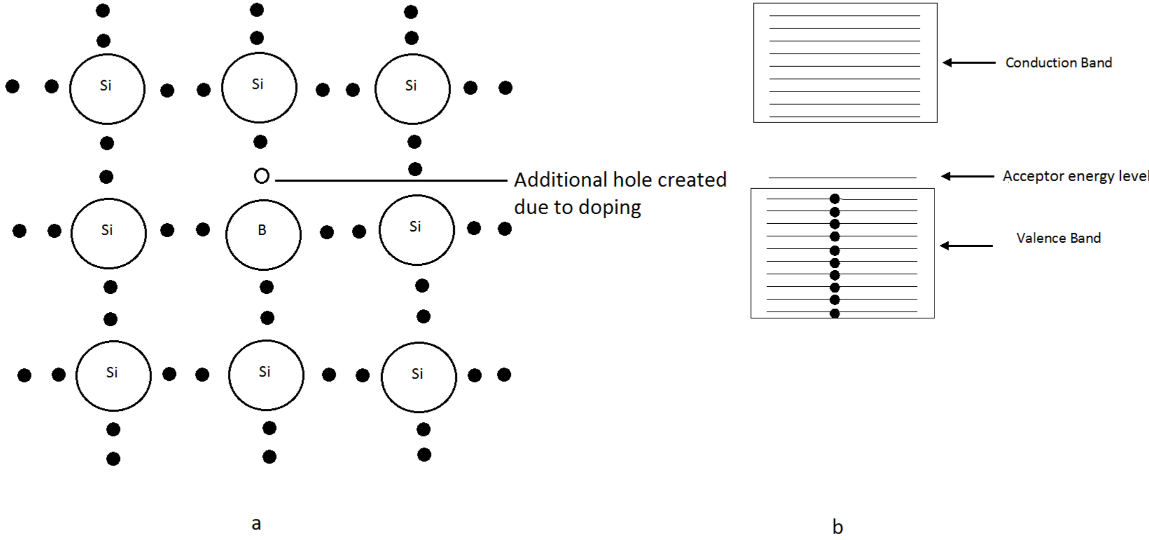

Figure 2.11: Extrinsic semiconductor (p type) a) Atomic bonding b) Band diagram

1.11 eV and that of germanium is 0.67 eV, which explains the higher intrinsic carrier concentration of germanium than silicon at a given temperature. The silicon-germanium phase diagram is depicted in figure 2.12.

2.2 Single crystal growth techniques

Depending upon the extent of the regularity exhibited in the atomic arrangement, crystalline solids can be classified as polycrystalline and single crystals. In the single crystal solids, the atomic orderliness extends throughout the material. The majority of the crystalline solids exist in polycrystalline form [24]. However, solids in single crystal form can be useful for various applications because of their properties. In particular, semiconductor single crystal material forms the backbone of the the modern electronics industry [24].

Based on the size of the grown single crystal, single crystal growth techniques are categorized as bulk and epitaxial growth techniques. In the former family of growth techniques, the size of the grown crystal is on the order of millimeters while in the latter it is on the order of sub-millimeters [15]. Si_xGe_{1-x} finds application both as an epitaxial layer and in the bulk crystal form. Some of its applications are hetero-junction bipolar transistors, photodetectors, thermo generator, and solar cell [26–30]. For semiconductors, two

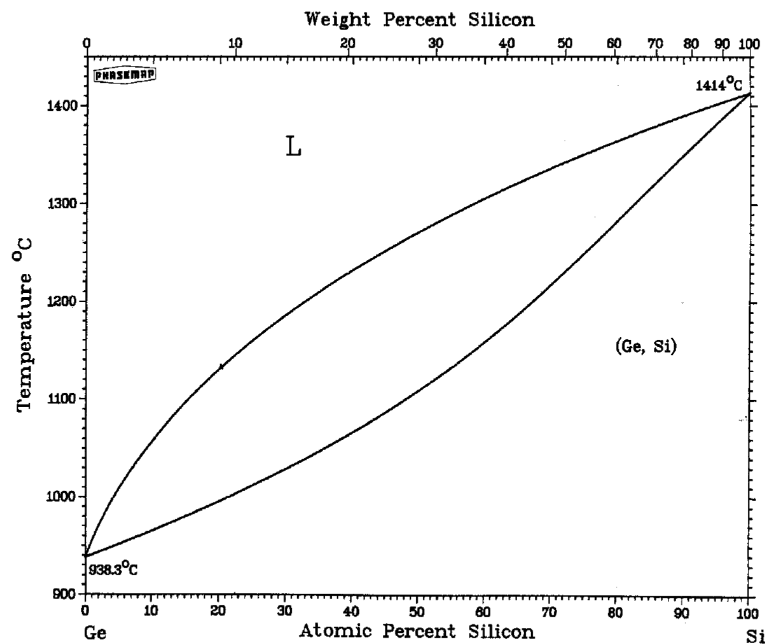

Figure 2.12: Phase diagram of silicon germanium [25]

commonly used single crystal growth methods are described below:

- Melt growth method- In this method, crystal growth is achieved by cooling the molten material below its melting point. Most of the semiconductor single crystals are grown by this method. Some of the commonly employed melt growth techniques are discussed very briefly below:
  - Czochralski- Named after its inventor, this is the most established and widely used growth technique for elemental semiconductors. A seed crystal is dipped into the melt contained in a crucible and then gradually pulled upwards at a controlled rate leading to single crystal growth. The diameter of the grown crystal is controlled by pull speed and temperature of the melt. Both seed and melt are rotated in opposite directions (figure 2.13) . Chief merits of this technique include [15]:
    * Growing crystal does not come in contact with crucible
    * High growth rates
    * Large diameter crystals
  - Vertical Bridgman- This technique uses a crucible in which the

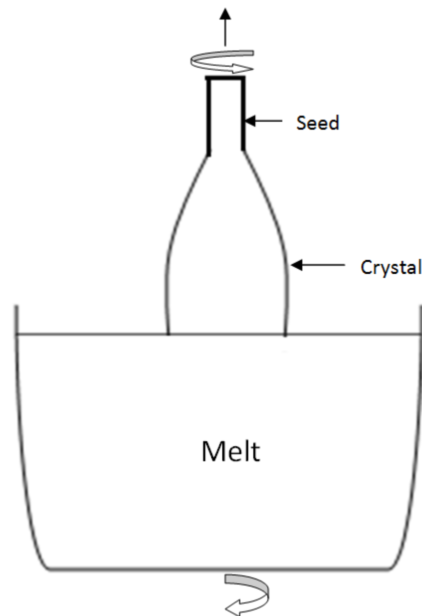

Figure 2.13: Schematic diagram of Czochralski crystal growth

entire charge is melted by subjecting it to a temperature gradient. The crucible is moved relative to the temperature gradient thereby leading to crystal growth through directional solidification. A schematic diagram of this technique is shown in figure 2.14 .

- Vertical Gradient Freeze- It works on a similar principle as that of vertical Bridgman with the only difference that the crucible is kept stationary and the temperature gradient is moved to achieve the directional solidification.
- Zone Melting- This technique involves the creation of a localized molten zone unlike other techniques discussed before in which the entire charge is melted [31] . This localized zone is moved through the entire charge with melting taking place at the leading edge and growth at the trailing edge.

- Solution Growth Method- In this method, a solution is prepared by dissolving the material which is to be crystallized in a suitable solvent which may or may not be part of the final crystal [32]. Crystal growth occurs due to the saturation and precipitation of the solution which in turn is accomplished in different ways depending upon the particular technique used. An inherent advantage of solution growth over melt

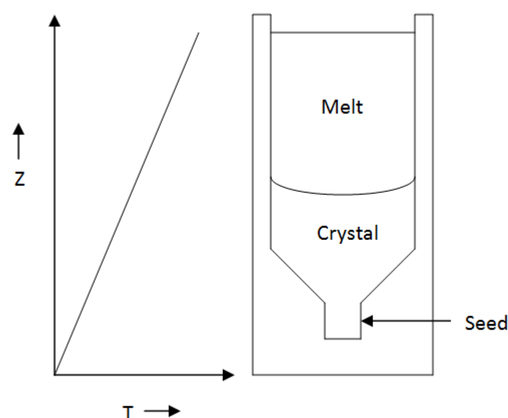

Figure 2.14: Schematic diagram of Vertical Bridgman and its temperature profile

growth is that by choosing an appropriate solvent, significant reduction in the growth temperature can be accomplished as it relies on dissolution rather than melting [32]. This method can be especially useful in case the crystal material has properties such as in-congruent melting, high vapour pressure, and high volatile contents but it suffers from disadvantages like slower growth rates compared to melt growth, solvent inclusion etc [32]. Some of the solution growth techniques are briefly discussed below [33]:

- LPD- Since this work is based on the numerical simulation of LPD, this technique is described in detail in the section 2.4.
- Travelling Heater Method (THM)-This technique is the solution growth counterpart of the zone melting technique. It involves the creation of a localized solution zone by using a temperature jump in that region which is then moved relative to the sample to move the zone. Dissolution takes place at the leading edge and precipitation takes place at the trailing edge due to saturation caused by the transport of solute across the zone from leading to trailing edge. Although the growth rate is quite small, on the order of 2mm/day, still this technique is used on a commercial scale to produce cadmium telluride crystals as melt growth technique is unsuitable to grow its crystals because of its high vapour pressure [15]. A schematic diagram of THM is shown in figure 2.16.
- Liquid Phase Epitaxy (LPE) and Liquid Phase Electro Epitaxy (LPEE)- The LPE technique relies on saturating the solution by

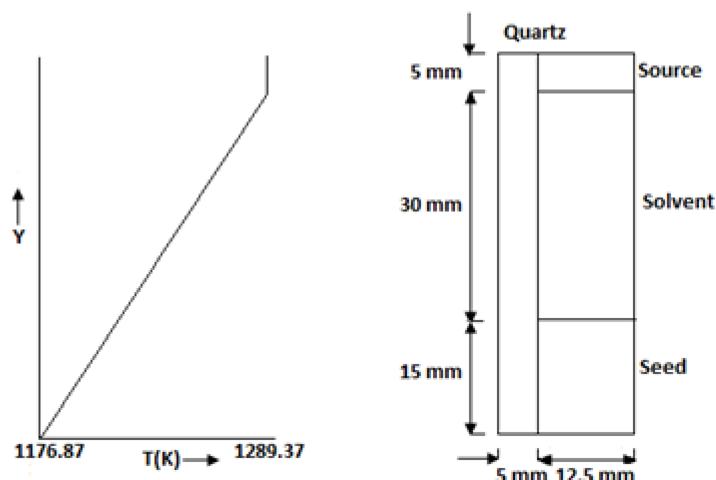

Figure 2.15: Schematic diagram of LPD growth technique (left half domain shown) and its temperature profile

decreasing its temperature whereas in LPEE electric current is passed through the solution to induce localized cooling in the form of Peltier cooling and also results in electromigration. Peltier cooling and electromigration are the principal mechanisms responsible for saturation and precipitation in LPEE. However, passing of electric current also results in Joule heating throughout the configuration and Peltier heating at the source- solution interface in case current passes through the source material. Peltier heating can be avoided by bypassing the electric current through the source material.

2.3 Issues with established melt growth techniques for growing Si_xGe_{1-x}

Various melt growth techniques have been used to grow Si_xGe_{1-x} . However, growing uniform composition Si_xGe_{1-x} crystals with the established melt growth techniques continues to be a challenge. The melting point of silicon is around 1414 ºC while that of germanium is around 938 ºC. Due to this wide disparity in the melting points, the liquidus and the solidus lines are extremely temperature sensitive and minor changes in the temperature can result in relatively large changes in the composition of the growing crystal [1]. Secondly, the solid state solubility of silicon in germanium is greater

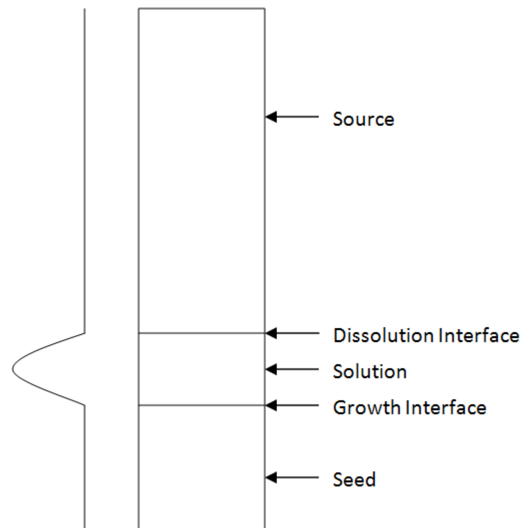

Figure 2.16: Schematic diagram of THM and its temperature profile

than the liquid state solubility and during the solidification process the melt is depleted in silicon due to its movement into the crystal across the growth interface and requires a silicon feeding mechanism to grow uniform composition crystals [1].

2.4 Liquid Phase Diffusion growth technique

This technique was originally developed as a variant of multicomponent zone melting growth and was utilized to grow bulk Si_xGe_{1-x} crystals comprising of a graded region (from x=0 to x=0.02) followed by a uniform composition region with x=0.02 [2]. Subsequently this technique, was named as "LPD" [3] and was used to grow graded bulk crystals from the germanium rich side . LPD, being a solution growth technique, is based on the principle of saturation and precipitation, unlike the melt growth technique in which solidification is achieved by cooling the melt below its melting point. The growth crucible in this technique consists of a stack of three regions (figure 2.15): a single crystal seed material (germanium) at the bottom, a polycrystalline source material (silicon) at the top, and a polycrystalline solvent material (germanium) sandwiched between the seed and the source. This configuration is then subjected to an axial temperature gradient in such a way that the solvent material (germanium) melts completely and the seed (germanium) melts partially and establishes the initial growth interface. The

source material (silicon) remains solid because of its higher melting point, and its contact surface with the silicon-germanium solution (initially the germanium melt) forms the dissolution interface. The dissolved silicon, according to the phase diagram, is transported in the solution by diffusion towards the melt-crystal interface (growth interface). The solubility in the melt is controlled by the local temperature. Under the applied axial temperature gradient, the temperature in the immediate vicinity of the growth interface is the lowest and accordingly the solubility is the lowest in this region. Due to the incorporation of silicon into the melt, the melt becomes a silicon-germanium solution and supersaturates near the growth interface, and growth of silicon-germanium crystal with a graded silicon composition begins. The growth continues with time with increasing silicon composition until the process is terminated.

To illustrate the LPD growth process consider the schematic phase diagram of silicon germanium shown in figure 2.17. The temperature of the initial growth interface corresponds to the melting point of germanium. The solution region in the immediate vicinity of the initial growth interface will correspond to point A. As silicon dissolves and is transported to the growth interface, the local silicon concentration starts increasing. Since the temperature is the lowest in this region in comparison to the rest of the melt, the solubility is lowest in this region indicated by point B. As the solution gets saturated in this region precipitation starts in the presence of the seed crystal which results in crystal growth. The applied temperature gradient results in directional solidification with the growth commencing near the seed crystal and proceeding in the upward direction. As the growth proceeds in the upward direction, it requires much higher amount of silicon (for instance corresponding to point E for a particular region in the solution) to saturate the solution. Another important aspect that can be observed from figure 2.17 is the significant difference in the silicon solid state and liquid state solubility. This means that as the growth proceeds silicon moves from the solution into the growing crystal across the growth interface. This depletion of silicon in the solution is compensated by continuous source of silicon supply at the dissolution interface. It has been shown experimentally [3] as well as numerically [10] that the interface shape is initially concave and its curvature increases as the growth proceeds and then flattens out. From a practical point of view, one of the major challenges associated with this technique is imposing the correct temperature profile so that the seed material does not melt completely and it can require a fair number of experiments before a perfect temperature profile can be obtained [3].

A significant amount of experimental and numerical work has been done

on LPD at the Crystal Growth Laboratory, University of Victoria. As already mentioned this technique was used in the work [3] to grow graded Si_xGe_{1-x} single crystals and a numerical model was developed in reference [10] to examine the role of natural convection in this growth technique. It was found that the natural convection was really strong during the early hours of growth after which the transport of silicon was diffusion dominated. Motivated by this finding, a numerical study was undertaken in reference [18] to investigate the effectiveness of a static magnetic field in suppressing the natural convection. It was found that a static magnetic field of 0.3 T was sufficient to suppress the natural convection currents but did not alter the shape of the growth interface dramatically. In the same work, the effect of rotating magnetic field (RMF) was investigated and it was found that RMF improved the radial compositional uniformity and a magnitude of 3 mT was sufficient to make the interface shape flat. This was followed by the numerical study of the combined influence of rotating and static magnetic fields on LPD [19] and it was shown that this combination resulted in essentially diffusive transport with homogeneous composition in the radial direction. The suitability study of the smoothed particle hydrodynamics (SPH) method to model the LPD process was carried out in the work [11]. Although some promising results were obtained, it was found that incorporating fluid flow in the SPH model would make it extremely computationally demanding. Further efforts were made to improve the ability of SPH to model the LPD process by using an implicit time stepping scheme which allowed the usage of much larger time steps thereby making it possible to carry out the simulations for much longer time periods [12]. Based on the numerical findings of the effect of magnetic field on the LPD growth technique, an experimental study was carried out in references [20, 23] examining the influence of static, rotating, and combined magnetic field on this growth process. It was found that the static magnetic field reduced the mass transport significantly and also had an impact on the temperature distribution [20]. Application of RMF had a beneficial effect on this growth method in terms of improving the growth rate considerably and it was found that the application of RMF alone was a better choice than using a combined field [23].

The dissolution process of silicon into germanium melt is an important part of the LPD growth technique and has been studied extensively both experimentally and numerically [34–41]. The effect of the position of the silicon source w.r.t. gravity as well as the role of the free surface was studied experimentally [34]. It was found that with the silicon source at the bottom significantly higher amount of silicon was dissolved in comparison to the case when the source was at top due to the solutal buoyancy effects [34]. A dis-

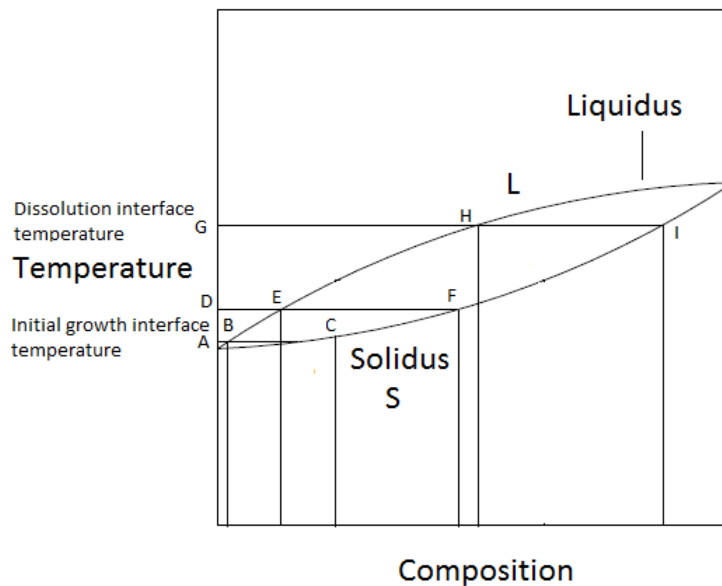

Figure 2.17: Illustration of LPD growth technique

solution study was carried out in slender crucibles to restrict the transport mechanism to diffusion in [35] and the temperature dependence of dissolved height was investigated. It was concluded that the diffusion coefficient was independent of the temperature for the investigated range of temperature [35]. A finite element based numerical simulation study was carried out in reference [36] and it was found that for the configuration of the silicon source at the top, transport was diffusion dominated and was in line with the previous experimental findings. The effect of a static magnetic field on dissolution with the silicon source positioned at the bottom was investigated experimentally [37] and it was discovered that the applied static field enhanced the silicon dissolution rate due to the modified flow structure in the melt. In another experimental work [38], the effect of static magnetic field on dissolution with source at top (similar configuration to that of LPD) was studied and the key finding was that dissolution interface shaped changed dramatically from being flat (without magnetic field) to curved into the source near the crucible wall (with magnetic field) which in turn was reasoned due to change in flow structure in the presence of magnetic field. Numerical studies on the effect of a static magnetic field on dissolution were performed in references [40, 41] and its effect on concentration field was examined.

2.5 OpenFOAM and Finite Volume Discretization

In the first part of this research work, an open source CFD toolbox called OpenFOAM [42] (Field Operation and Manipulation) was utilized as it offers the flexibility to develop a customized solver for a specific application. It is basically a C++ class library and makes extensive use of object oriented principles to solve problems in computational continuum mechanics and is based on the finite volume discretization technique [43]. This section is based on the work [44, 45] and the reader should consult it for further details.

Discretization in this context implies:

- Spatial Discretization or Mesh generation
- Temporal Discretization
- Equation Discretization

OpenFOAM uses a cell centered, co-located variable storage arrangement and is a segregated solver which means that equations are solved one at a time and inter-equation coupling is treated in an explicit manner. The purpose of any discretization method is to convert the field equation(s) (usually one or more partial differential equation) into a system of algebraic equations whose solution gives an approximate solution to the original field equation(s) at discrete locations in space and time. In FVM, Gauss identities are used while discretizing the field equation(s) and are listed below:

$$\int_V \nabla \cdot \mathbf{a} dV = \oint_{\partial V} d\mathbf{S} . \boldsymbol{a} \tag{2.6}$$

$$\int_V \nabla \phi dV = \oint_{\partial V} d\boldsymbol{S} \phi \tag{2.7}$$

$$\int_V \nabla \mathbf{a} dV = \oint_{\partial V} d\mathbf{S}\, \mathbf{a} \tag{2.8}$$

where ∂V is the closed surface enclosing the volume V

$$(\nabla \cdot \mathbf{a})\, V_P = \sum_{\mathrm{f}} \mathbf{S} \cdot \mathbf{a_f} \tag{2.9}$$

As per the OpenFOAM spatial discretization, cell faces can be divided into two groups namely internal faces and boundary faces. The face area

vector $\mathbf{S}_f$ is constructed in such a way that it points outwards from the cell with lower label (called the "owner" cells) and towards the cell with higher label (called the "neighbour" cells). In the equation 2.9, $\mathbf{S}$ represents the normal surface area pointing outwards of the face. Thus, a correction has to be applied for all the "neighbour" cells. So, the R.H.S of equation 2.9 can be rewritten as:

$$\sum_{\text{f}} \mathbf{S} \cdot \mathbf{a_f} = \sum_{\text{owner}} \mathbf{S_f} \cdot \mathbf{a_f} - \sum_{\text{neighbour}} \mathbf{S_f} \cdot \mathbf{a_f} \tag{2.10}$$

The discretization procedure using FVM is explained with standard transport equation as an example. The general transport equation can be written as

$$\underbrace{\frac{\partial \rho \phi}{\partial t}}_{Transient\,term} + \underbrace{\nabla \cdot (\rho \mathbf{U} \phi)}_{Convection\,term} = \underbrace{\nabla \cdot (\rho \Gamma \nabla \phi)}_{Diffusion\,term} + \underbrace{S_\phi}_{Source\,term} \tag{2.11}$$

As per the FVM , this equation is integrated over each control volume and time

$$\int_t^{t+\Delta t} \left[\int_{V_P} \frac{\partial \rho \phi}{\partial t} dV + \int_{V_P} \nabla \cdot (\rho \mathbf{U} \phi) dV \right] dt = \int_t^{t+\Delta t} \left[\int_{V_P} \nabla \cdot (\Gamma \nabla \phi) dV + \int_{V_P} S_\phi dV \right] dt \tag{2.12}$$

2.5.1 Convection term

Using equation 2.9, the convection term can be written as

$$\begin{aligned} \int_{V_P} \nabla \cdot (\rho U \phi) &= \sum_f \mathbf{S} \cdot (\rho \mathbf{U} \phi)_f \\ &= \sum_f \mathbf{S} \cdot (\rho U)_f \phi_f \\ &= \sum_f F \phi_f \end{aligned} \tag{2.13}$$

$$F = \mathbf{S} \cdot (\rho \mathbf{U})_f \tag{2.14}$$

Thus it can be seen that discretization of the convection term requires the knowledge of mass flux at the face centres. Usually, the flow field is unknown and it requires the solution of the Navier-Stokes equation. But even if it is assumed to be known then also we still need to make an assumption about the variation of ϕ in between the cell centres, as we need its value at the face centres. Depending upon the specific profile function assumption, different convection differencing schemes exist. Two of the most common schemes are discussed below:

- Central Differencing Scheme- This scheme assumes a linear variation of the transport variable between the adjacent cell centres across each face. It is second order accurate but can lead to spurious oscillations in the solution in a convection dominated flow. However, it is well suited for low Peclet number flow regimes.
- Upwind Differencing Scheme- This scheme as the name says, assumes the value of the transport variable at the face to be same as that at the cell centre in the upstream direction. It is first order accurate and is prone to numerical diffusion

$$\phi_f = \begin{cases} \phi_P & if\, F \geq 0 \\ \phi_N & if\, F < 0 \end{cases} \tag{2.15}$$

2.5.2 Diffusion Term

$$\begin{aligned} \int_{V_P} \nabla \cdot (\rho\Gamma\nabla\phi) dV &= \sum_f \mathbf{S} \cdot (\rho\Gamma\nabla\phi)_f \\ &= \sum_f (\rho\Gamma)_f \mathbf{S} \cdot (\nabla\phi)_f \end{aligned} \tag{2.16}$$

For orthogonal meshes, (i.e the vector joining the cell centres is parallel to the surface area vector) the following expression can be used.

$$\mathbf{S}.(\nabla\phi)_f = |\mathbf{S}| \frac{\phi_N - \phi_P}{|\mathbf{d}|} \tag{2.17}$$

An alternative approach is to calculate the gradient expression at the cell centre and interpolate it

$$(\nabla\phi)_P = \frac{1}{V_P}\sum_f \mathbf{S}\phi_f \tag{2.18}$$

$$(\nabla\phi)_f = f_x(\nabla\phi)_P + (1 - f_x)(\nabla\phi)_N \tag{2.19}$$

where f_x is the interpolation factor defined as $\frac{f\bar{N}}{\bar{PN}}$

2.5.3 Source Term

The terms which are not part of temporal derivative, convection and diffusion terms are placed into a generic term called the source term. Source term, in general can be a function of the transport variable and in that case, this relationship needs to be linearized if it is a non linear function of ϕ

$$S_\phi = S_I\phi + S_E \tag{2.20}$$

$$\int_{V_P} S_\phi(\phi)dV = S_I\phi_P V_P + S_E V_P \tag{2.21}$$

2.5.4 Temporal Discretization

Substituting equation 2.13 , 2.16, 2.21 in equation 2.12 we get,

$$\int_t^{t+\triangle t}\left[\left(\frac{\partial\rho\phi}{\partial t}\right)_P V_P + \sum_f F\phi_f - \sum_f(\rho\Gamma)_f\mathbf{S}.(\nabla\phi)_f\right]dt = \int_t^{t+\triangle t}(S_I\phi_P V_P + S_E V_P)dt \tag{2.22}$$

$$((\rho_P\phi_P)^n - (\rho_P\phi_P)^{n-1})V_P + \int_t^{t+\Delta t}\left[\sum_f F\phi_f - \sum_f(\rho\Gamma)_f\mathbf{S}.(\nabla\phi)_f\right]dt = \int_t^{t+\Delta t}(S_I\phi_P V_P + S_E V_P)dt \tag{2.23}$$

An assumption has to be made regarding the variation of ϕ_P w.r.t time. Depending upon the specific choice of the function, different discretization schemes exist and are discussed briefly below:

- Explicit- In this case, the old time field is assumed to exist throughout the time step except at the end. It is first order accurate in time and becomes unstable if the Courant number exceeds 1 which is defined as follows:

$$Co = \frac{\mathbf{U_f} \,.\, \mathbf{S}}{\mathbf{d} \,.\, \mathbf{S}} \triangle t \tag{2.24}$$

This puts a serious limitation on the maximum time step size even for a moderately fine mesh.

- Implicit(Euler Implicit)-This scheme assumes that the current time step value exists throughout the time step except at the beginning. It is first order accurate but is unconditionally stable. Using this scheme, the discretized equation is given by:

$$\frac{\phi_P^n - \phi_P^{n-1}}{\triangle t} V_P \rho_P + \sum_f F \phi_f^n - \sum_f (\rho \Gamma_\phi)_f \mathbf{S}.(\nabla_f \phi^n) = (S_I \phi_P^n V_P + S_E V_P) \tag{2.25}$$

- Crank-Nicholson- This scheme assigns equal weights to the current and old time step value. It can give physically unrealistic results.

2.5.5 Solution of system of linear algebraic equations

A system of linear equations is generated by discretization of the transport equation with one equation for each cell. It can be expressed in a general form as follows:

$$a_P \phi_P^n + \sum_N a_N \phi_N^n = R_P \tag{2.26}$$

and can be expressed in the matrix form as follows:

$$[A][X] = [R] \tag{2.27}$$

Terms which are treated implicitly contribute to the matrix coefficients and may contribute to the source vector. On the other hand, explicit terms contribute only to the source vector. Numerical techniques for solving system of linear algebraic equations can broadly be classified as direct and iterative techniques. Iterative solvers are usually preferred over direct solvers because they are computationally less demanding. However, they impose additional requirements on the matrix structure to ensure convergence. Scarborough criterion (i.e. matrix is diagonally dominant) is a sufficient but not necessary condition for the convergence of iterative methods.

Chapter 3

Numerical simulation of the LPD growth technique using a fixed grid approach

3.1 Introduction

Physically, bulk crystal growth is characterized by various processes occurring at various scales which makes an "all inclusive" model computationally prohibitive [46]. Based on the overall modeling objectives, models can be classified as " process" models and "defect" models which relate the crystal defects to the process conditions [47]. Another frequently encountered term in this field is that of the "global" models, signifying a class of models in which furnace heat transfer is part of computation instead of relying on boundary conditions to account for these effects (see for instance reference [48]). Although significant progress has been made in modeling of transport phenomena in crystal growth, it still continues to be a challenging problem because of various complexities involved including the issue of changing geometry inherent to the growth process [49]. There are various numerical techniques available to tackle the moving boundary problem. Broadly these techniques fall into two categories, namely Lagrangian which utilize an interface adjusting moving grid, and Eulerian which are based on a fixed grid approach and the interface position is obtained as part of the solution [50]. While each of these two approaches has its own pros and cons, the biggest advantage of the fixed grid approach lies in its relative simplicity. The basic idea of this approach is to represent the entire domain by a single set of field equations.

3.2 Model description

From a numerical simulation perspective, the LPD growth process consists of two main steps, namely melting and solidification. Models used for simulating each of these two sub-processes along with the assumptions made are discussed below:

Assumptions

- The effect of natural convection in the silicon-germanium melt (solution) was neglected as the simulation was carried out for zero gravity condition.
- Enthalpy of mixing associated with the dissolution of silicon into the silicon-germanium melt was neglected as silicon and germanium form nearly a ideal solution.
- Local thermodynamic equilibrium was assumed at the dissolution and growth interfaces. The dissolution interface was considered to be stationary as its velocity is very small in comparison to the growth velocity.
- The silicon-germanium solution (melt) was assumed to be dilute in terms of the silicon concentration. Fourier's law and Fick's law were used to describe the heat and mass fluxes respectively.
- Soret and Dufour effects were not taken into account.
- The coefficients of thermal and mass diffusivities were assumed to remain constant with temperature.
- Mass diffusivity of silicon in solid germanium is small in comparison to that of the germanium melt, thus was not taken into account.
- The system was considered to be axisymmetric

3.2.1 Modeling the melting process of germanium

The well known enthalpy-porosity method [4] was used to model the melting of pure germanium. In this method, a single set of field equations is used to model the entire domain(molten and solid). The interface is computed as part of the solution rather than tracking it explicitly. To account for the absorption of latent heat during the melting process, a sink term is added to the energy equation. Depending upon the manner in which the liquid fraction is updated after each time step there are two variants of this method called the T-based and the H-based methods [50]. In the T-based method,

the liquid fraction for each cell is updated based on its temperature but the update expression assumes that a phase change occurs over a range of temperature which is not realistic for phase change of pure components which undergo an isothermal phase change. The H-based method uses an inverted enthalpy-temperature relationship, i.e. it uses T=T(H) rather than H=H(T). Since the temperature is a continuous function of the enthalpy for the phase change process unlike the enthalpy which is a discontinuous function of the temperature, thus it eliminates the need to make the assumption that the phase change occurs over a range of temperature and is well suited for modeling the phase change of pure components and hence was the algorithm of choice in the present work.

3.2.2 Modeling the solidification of Si_xGe_{1-x}

As described earlier, solidification in the LPD process occurs due to saturation and precipitation. Consequently, this rules out the possibility of using the conventional enthalpy method which is well suited to model the solidification process in melt growth driven by cooling of the melt. However, there exists a possibility to model the LPD growth using a virtual front tracking model [51] developed for modeling dendritic growth since in this process like the LPD growth, solidification is considered to be driven by the difference in the local solubility and the actual composition and therefore was utilized in this work. As per this model, solidification in a cell is predicted when the actual concentration in the cell exceeds the equilibrium concentration of silicon computed from the phase diagram corresponding to the local temperature. Release of latent heat during solidification is accounted for in a similar way as in the enthalpy method i.e. by including a source term in the energy equation. In addition, there is transport of silicon from the melt into the crystal across the solidification front because of higher solid-state solubility of silicon in solid germanium than in liquid germanium. This decrease of silicon concentration in the melt as solidification proceeds is accounted for by including a sink term in the mass transport equation.

3.2.3 Choice of the CFD solver

To solve the discretized governing equations, one of the options is to develop the source code from scratch. Although this approach gives the maximum flexibility and complete control but has a very high developmental time and requires extensive validation studies before confidence can be gained on the

accuracy of the results. A second choice is to use an established commercial CFD code such as Ansys Fluent but implementing a new solution algorithm in these codes is not possible as the user does not have any access to the source code. Finally, a third option is to use an open source code such as OpenFOAM which gives complete access to the source code and has a very large user-base in the CFD community. OpenFOAM was chosen to develop the solver for implementing this new solution methodology as it offers almost the same flexibility as that of one's own code while substantially reducing the developmental time. Further, because of its widespread usage in the field of CFD, its code has been extensively tested and hence it offers the accuracy and credibility comparable to that of any of the established commercial CFD code.

3.2.4 Numerical solution domain

The numerical solution domain consists of the solid Ge seed at the bottom, silicon-germanium solution (initially germanium melt) in the middle, the silicon solid source at the top, and the wall of the quartz ampoule. Half the domain and the applied temperature profile are shown in figure 2.15 . OpenFOAM [42] always uses the three dimensional cartesian coordinate system, and for simulating a two-dimensional axisymmetric case the geometry should be specified as wedge with a small angle ($<5^0$). To keep the interface thickness small, a fine mesh was employed in the melt region (10 mesh elements per mm) whereas a relatively coarse mesh was used for source and quartz region (5 mesh elements per mm) for computational efficiency. This mesh size was arrived at after performing the grid independence study.

3.2.5 Field equations

Two different sets of field equations (comprising of the energy and the mass transport equations) were solved corresponding to the melting and solidification models. The energy equation was solved for the entire domain whereas the mass transport equation was solved only for the melt region.

3.2.5.1 Melting Process

In the melt, the only field equations are the energy balance and mass transport equations since the contribution of fluid flow was neglected. As already mentioned earlier the interfacial effect of absorption of latent heat of fusion is

taken into account by adding a sink term to the energy equation.The energy balance yields the following equation:

$$\frac{\partial T}{\partial t} = \alpha \nabla^2 T - S_T \tag{3.1}$$

The thermal diffusivity of a cell is computed based on the value of the liquid fraction of that cell. Once a cell becomes completely liquid its thermal diffusivity is changed to its liquid state value from its solid state value.

$$\alpha = \begin{cases} \alpha_s & if \quad \epsilon < 1 \\ \alpha_l & if \quad \epsilon = 1 \end{cases} \tag{3.2}$$

The sink term to account for latent heat effects is computed as follows:

$$S_T \equiv \frac{L}{c_p} \frac{\partial \epsilon}{\partial t} \tag{3.3}$$

$$\frac{\partial C}{\partial t} = D \nabla^2 C \tag{3.4}$$

Mass diffusivity is updated using a similar approach used for updating the thermal diffusivity.

$$D = \begin{cases} D_s & if \quad \epsilon < 1 \\ D_l & if \quad \epsilon = 1 \end{cases} \tag{3.5}$$

Enthalpy of a computational cell is calculated based on its temperature and liquid fraction which in turn is used to compute the liquid fraction of the cell.

$$H_P^n = c_p T_P^{n-1} + \epsilon^{n-1} L \quad and \quad \epsilon^n = \begin{cases} 0 & if \quad H_P^n < H_s \\ \frac{H_P^n - H_s}{H_l - H_s} & if \quad H_s \leq H_P^n \leq H_l \\ 1 & if \quad H_P^n > H_l \end{cases} \tag{3.6}$$

3.2.5.2 Solidification Process

As described earlier the release of latent heat is accounted by adding source term to the energy equation and depletion of silicon in the melt during solidification is accounted by adding sink term to the mass transport equation.

$$\frac{\partial T}{\partial t} = \alpha \nabla^2 T + S_T^{'} \quad and \quad \frac{\partial C}{\partial t} = D\nabla^2 + S_C \tag{3.7}$$

The source and sink terms are calculated as follows:

$$S_T^{'} \equiv \frac{L}{c_p}\frac{\partial \gamma}{\partial t} \quad and \quad S_C \equiv C(1-K)\frac{\partial \gamma}{\partial t} \tag{3.8}$$

The thermal diffusivity and mass diffusivity are updated based on the value of solid fraction. Once a cell becomes completely solid its thermal and mass diffusivities are changed from their liquid state values to solid state values.

$$\alpha = \begin{cases} \alpha_l & if \quad \gamma < 1 \\ \alpha_s & if \quad \gamma = 1 \end{cases} \quad and \quad D = \begin{cases} D_l & if \quad \gamma < 1 \\ D_s & if \quad \gamma = 1 \end{cases} \tag{3.9}$$

Lever rule is used to calculate the mass fraction solidified in a given time step while the actual mass fraction solidified is computed from a different expression as follows:

$$\Delta\gamma_{lever} = \frac{C^{N-1} - C_l^{N-1}}{C_s^{N-1} - C_l^{N-1}} \quad and \quad \Delta\gamma^N = min(\Delta\gamma_{lever}^N,\ 1 - \sum_{N=1}^{N_T-1} \Delta\gamma_{lever}^N) \tag{3.10}$$

The cumulative mass fraction solidified is calculated as follows:

$$\gamma^N = \sum_{N=1}^{N} \Delta\gamma^N \quad and \quad \gamma^{N_T} = \sum_{N=1}^{N_T} \Delta\gamma^N = 1 \tag{3.11}$$

$$\frac{\partial T}{\partial t} = \alpha \nabla^2 T \tag{3.12}$$

The solidus and liquidus equilibrium composition is computed as follows:

$$C_l^{eq}(T) = 0.072075(T - 1211.87) \tag{3.13}$$

$$C_s^{eq}(T) = 0.336775(T - 1211.87) \tag{3.14}$$

$$K = \frac{C_s^{eq}}{C_l^{eq}} \tag{3.15}$$

$$-\lambda \nabla T = \beta\sigma(T^4 - T_{amb}^4) \tag{3.16}$$

3.2.5.3 Quartz wall and solid source

During both melting and solidification processes, in the quartz wall and solid source only the heat conduction equation with appropriate thermal diffusivity coefficients is solved:

$$\frac{\partial T}{\partial t} = \alpha \nabla^2 T \tag{3.17}$$

Property	Source(Silicon)	Seed (Germanium)	Solution/Melt	Crystal	Quartz
λ (W/mK)	23.7	20	42.8	20	2
ρ (Kg/m3)	2301.6	5323	5670	5323	2200
c_p (kJ/kg)	967	396.1	406	396.1	1200
D (m^2/s)	-	-	10^{-8}	-	-
L (kJ/kg)		466.5	466.5		
β	0.71	-	-	-	0.85
$\sigma(1/Wm)$	-	-	1.7 x 10^6		

Table 3.1: Thermophysical properties of SiGe system compiled from [10, 15, 52–54]

3.2.6 Solution algorithm

3.2.6.1 Melting solver

As mentioned earlier, the melting solver utilizes the H-based enthalpy-porosity method [50] and the solidification solver uses the algorithm proposed in reference [51].

1. Initialize the concentration field and the liquid fraction to zero in the melt sub-domain(seed and solvent region) and the temperature field to 298K in the entire domain. Also, initialize the thermal diffusivity to an appropriate value in each sub-domain.

2. Based on the previous time step value of the temperature and the liquid fraction, update the enthalpy of each cell using equation 3.6 -1.
3. Compute the liquid fraction for each cell using equation 3.6 -2.
4. Update the diffusion coefficient and the thermal diffusivity for each cell (equation 3.2, 3.5) and compute the source term for the energy equation (equation 3.3) which is dependent upon the rate of change of the liquid fraction.
5. Solve energy and mass transport equations (equation 3.1, 3.4, 3.17). If the melting process is complete, switch to solidification solver else increment the time and go to step 2.

3.2.6.2 Solidification solver

1. Initialize the concentration and the temperature fields to the values obtained from the melting solver and also identify the unmelted seed region in the melt sub domain.
2. Set the solid fraction to one in the unmelted region and to zero in the remaining melt sub domain. Check the state of each cell in the melt region. If it lies in the unmelted seed region or if it is a fully solidified cell ($\gamma = 1$) then it does not enter the solidification loop. For other cells in the melt region (i.e. $\gamma < 1$) proceed to step 3.
3. Using the latest value of temperature compute the liquid and solid state solubility of silicon and the partition coefficient for each cell (equation 3.13, 3.14, 3.15).
4. For each of these cells compare the latest concentration value and the liquid solubility. If the concentration has exceeded the liquid solubility in one or more cells adjoining the seed crystal/solidified crystal, then solidification starts in these cells and proceed to step 5 for these solidifying cells.
5. Compute the mass fraction solidified in this time step from the lever rule using equation 3.10-1 .
6. To prevent a cell from getting solidified completely in one step, the actual mass fraction is computed from equation 3.10 -2. Compute the cumulative sum of the mass fraction solidified for each solidifying cell using equation 3.11 .
7. As soon as a cell gets solidified completely (i.e.$\gamma = 1$) the concentration in a fully solidified cell is set to the local solid state solubility as per

equation 3.14.

8. Update the thermal diffusivity and the mass diffusivity in the melt region using equation 3.9.
9. Compute the source terms from equation 3.8.
10. Solve energy and mass transport equations 3.7 , 3.17 .
11. Check if the current time exceeds the maximum simulation time. If yes, then stop else increment the time and go to step2.

3.2.7 Numerical Solution

To solve the field equations, a top level code was written in OpenFOAM . It is important to note that the mass diffusivity of silicon in solid germanium is several orders of magnitude smaller than that in molten germanium. Also, the thermal diffusivity is different for the solid and the liquid phase. Therefore, care must be taken while discretizing the terms involving such variable properties. Consequently for the melt region of the domain, the mass and the thermal diffusivities were defined as field variables and harmonic interpolation [55] was used for discretizing the diffusion terms in the mass transport and the energy equation. The first order accurate Euler implicit scheme was chosen for temporal discretization. A constant time step of 2 sec was employed. The solution was considered converged when absolute residuals had fallen below the specified solver tolerance of 10^{-9}.

3.2.7.1 Boundary and Initial condition

With reference to figure 2.15 the following boundary conditions are used :

- Concentration field

1. Bottom and inner quartz walls are impermeable across which there is no transport of mass, which leads to zero normal gradient boundary condition.
2. On the dissolution interface, equilibrium was assumed, and the concentration was prescribed as a function of temperature from the phase diagram.
3. The liquidus and solidus curves were linearized for the temperature range of interest (1211.87-1289.12K). It is important to note that these

relations (equations 3.13, 3.14) give the solubility in atomic percentage whereas in other relations the concentration is expressed in mass fraction.

- Thermal field

1. Bottom- A constant temperature of 1176.87K was prescribed at the bottom.
2. Outer quartz wall-A linear temperature gradient of 2.5K/mm was specified along the solution zone and a constant temperature of 1289.37K along the source.
3. Top- The radiative heat loss from the top was taken into account by using equation 3.16 .

The concentration field was initialized to zero while the temperature field was initialized to a value of 298K. The values of physical properties used in the present work are listed in table 3.1.

3.3 Results and Discussion

The simulated crystal growth is shown in figure 3.1 (It must be noted that in all the presented results throughout the thesis the solution domain shown in figure 2.15 has been mirrored around the centreline for more clarity). Figure 3.2 depicts the computed temperature and concentration fields in the melt and the shape of the initial growth interface after one hour of simulation time. The computed isotherms of the present simulation are relatively in good agreement with the simulation results obtained using a dynamic grid approach [10]. However, the computed iso-concentration lines show slight differences compared with the experimental results of reference [3]. This difference in behaviour can be explained on the basis of the difference in the values of Prandtl and Schmidt numbers for the melt. Prandtl number for the melt is 0.0075 while the Schmidt number is around 7.67 [10]. Thus for a given Reynolds number the solutal Peclet number is greater than its thermal counterpart. This means that the advective mass transport is significant in comparison to the diffusive mass transport while the advective heat transport is negligible in comparison to the diffusive heat transport. Thus the heat transport does not change much in the presence of convection but mass transport is significantly affected by the inclusion of convective effects. The difference in the results using the fixed and dynamic grid approach is more prominent in the evolution of the growth interface that is shown in figure 3.3. Although the total growth thickness for a 29hrs growth period is very close

to those of the experiment results of reference [3], the simulation predicts slightly faster growth during the initial stages of growth as can be seen from figure 3.3 and table 3.2. The present simulation (on left in figure 3.3) under zero gravity predicts slightly faster initial growth (enhanced mass transport) compared with that of the simulation for the Earth-bound experiments (in middle in figure 3.3) in which, while the mass transport in the upper section of the melt was mainly diffusion dominated, in the bottom region of the melt near the growth interface there were strong convective cells. The faster initial growth along the crucible wall in the present simulation can be attributed to the lack of radial mixing owing to the absence of convection. This in turn leads to relatively cooler fluid near the crucible wall than in the interior melt in the vicinity of growth interface during the early hours of growth.

	Present Simulation	Experiments [3]	Simulation [10]
Total Growth Thickness (29hrs growth): centre	~19 mm	~19 mm	~17 mm
Total Growth Thickness (29hrs growth): near wall	~19 mm	~16 mm	~17 mm
Interface shape with respect to experiment	Flatter at the centre, sharper near the wall		Sharper near the wall
Evolution of interface with respect to experiment	Faster near the wall		Better agreement with experiment
Growth thickness at centre after 10hrs of growth	About 8 mm	About 7 mm	About 6 mm

Table 3.2: Comparison of growth thickness and interface evolution

For instance, as presented in table 3.2, in the simulation of the Earth-bound experiments the growth thickness is about 6 mm after ten hours of growth time while in the present simulation the interface reaches the position of 8 mm during the same period. The experimental value is about 7 mm for this period. The evolution of the growth interface presents a similar trend to

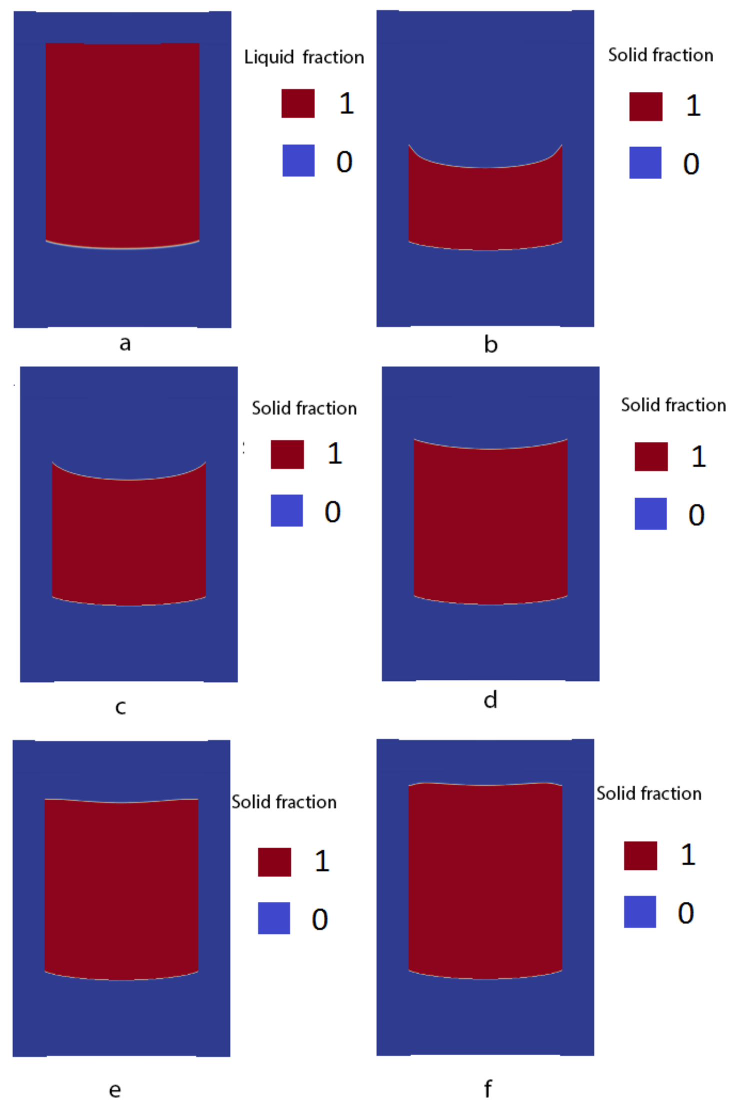

Figure 3.1: Simulated crystal growth at a) Initial position b) t=20 hrs c) t=40 hrs d) t=60 hrs e) t=80 hrs f) t=100hrs

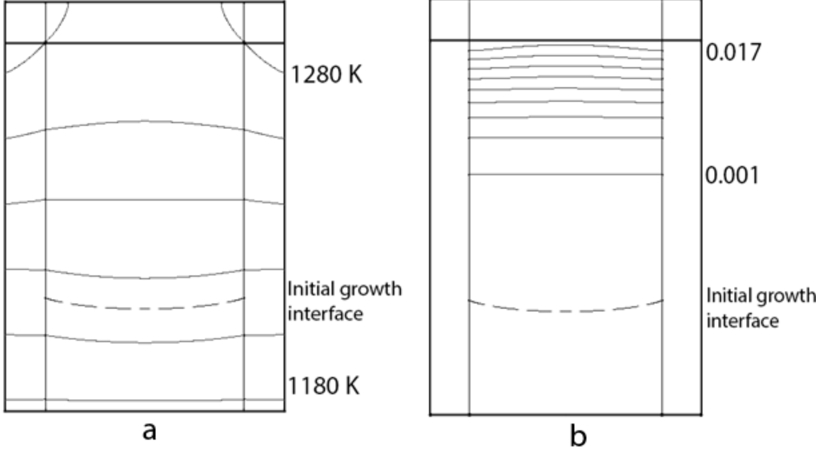

Figure 3.2: a) Isotherms at an interval of 20K and b) isoconcentration lines at an interval of 0.002 in the melt at t=1hr

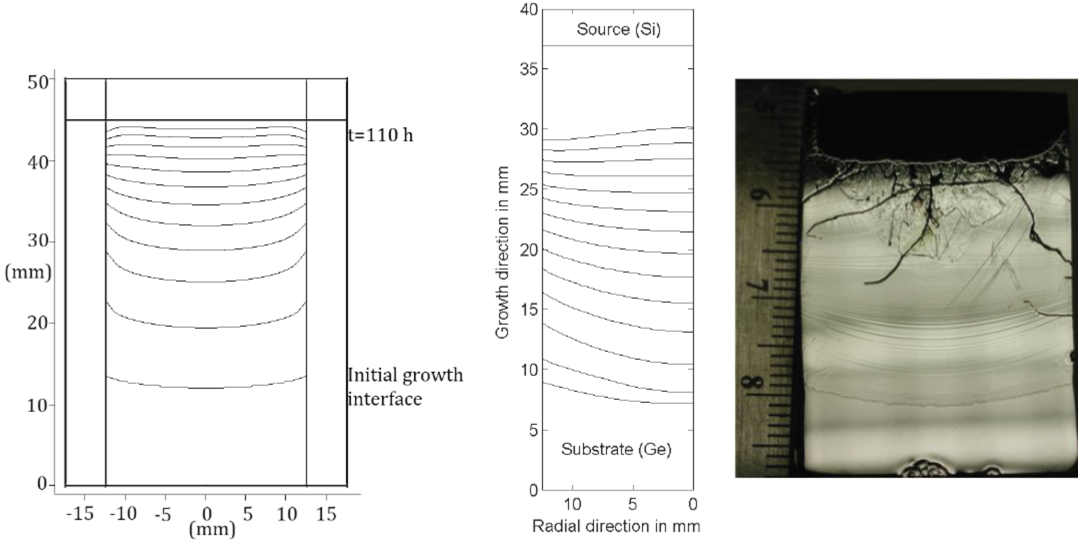

Figure 3.3: Computed evolution of the growth interface by the present simulation under zero gravity (on left, with time interval of 10hr in between each line). The simulation including convection [10] based on Earth-bound experiments (in middle, time interval between each line is 3hr (total of 39hr growth), only half zone is shown). The experimental results are shown on right [3] .

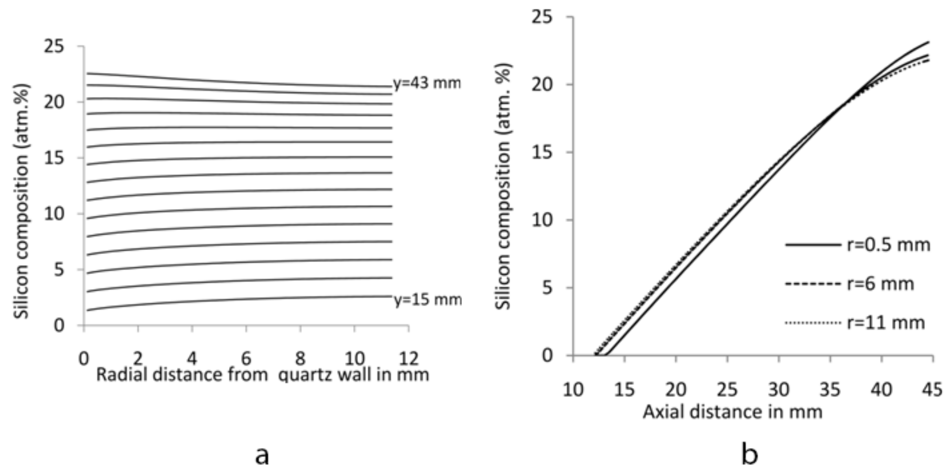

Figure 3.4: (a) Radial and (b) axial composition profiles for the simulated crystal growth at t=142hrs

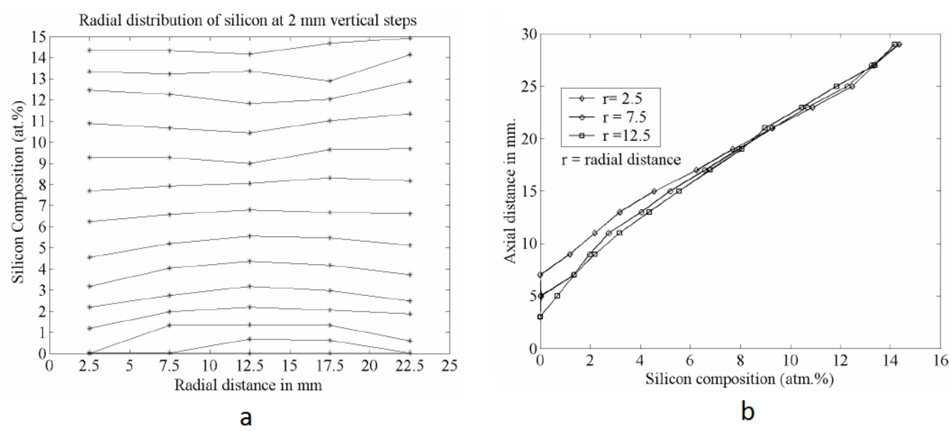

Figure 3.5: Experimentally measured a) Radial and (b) axial composition profiles [3]

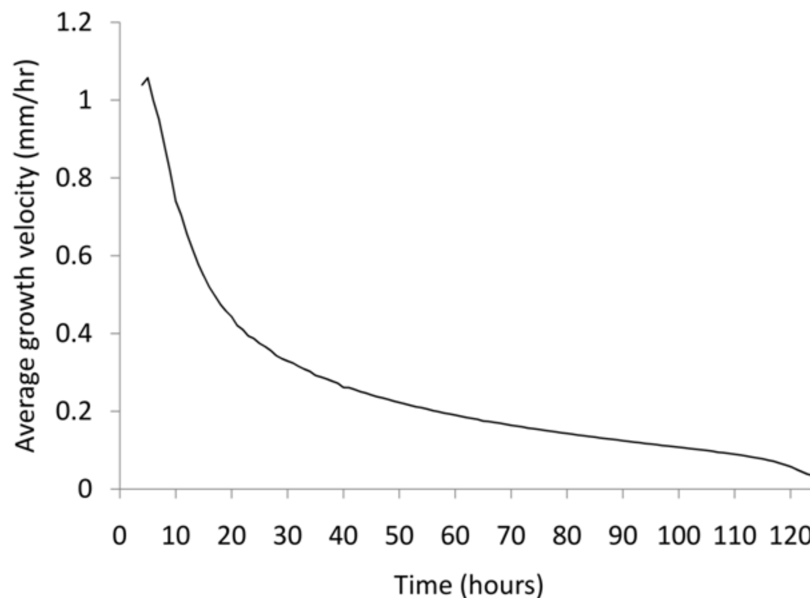

Figure 3.6: Variation of average growth velocity with time

that observed in the experiments and also those from the previous simulations, except that the flattening of the growth interface is delayed compared with that of experiments (as seen in figure 3.3 on left in comparison with those in the middle and on right), and also initially faster growth along the crucible wall. The initial concave growth interface slowly flattens as growth progresses, and finally becomes convex near the end of the growth process similar to the experiments. The computed averaged growth velocity profile under zero gravity is given in figure 3.6. As predicted from the experiments, the growth slows down as time progresses due to reduction in silicon dissolution into the growth melt since the temperature gradient is getting shallower in the growth direction. Although a faster initial growth is predicted under zero gravity, the trend of the interface evolution and the total growth thickness after twenty nine hour of growth agree with experiments. A well-designed LPD growth experiment (for silicon germanium) under microgravity may shed light on these numerical predictions. The computed axial and radial silicon composition profiles in the grown crystal are shown in figure 3.4. As seen in figure 3.5, these computed composition profiles are in qualitative agreement with the experimental results of reference [3]. Again, this implies that from a space experiment one may also expect a similar silicon distribution in the grown crystals; linear in the growth direction and almost uniform in the radial direction.

3.4 Inclusion of convective effects

The LPD growth system has an axially stabilizing density gradient because of the imposed axial temperature and concentration gradients which essentially means that the lighter fluid is at the top while the heavier fluid at the bottom. The solutal Grashof number for this system is 10.7 x 10^7while thermal Grashof number is 5.09 x 10^7, which means that the suppression of natural convection due to solutal gradient is stronger than its thermal counterpart [10]. However, during early hours of growth, solutal gradient is not completely established and is unable to suppress the natural convection near the growth interface due to radial temperature gradient [10]. Thus even though LPD growth is a diffusion dominated process but convection is quite strong during early hours of growth [10]. The present simulation methodology was used to simulate earth bound LPD growth which includes convective effects. However, the solidification model used in the solver was originally developed for low Peclet number transport regime in the reference [51]. So, the usage of this solidification model during early hours of growth is not valid and reliable results could not be obtained following this methodology.

3.5 Summary

This chapter focussed on the development of a fixed grid numerical solution procedure to simulate the LPD growth under zero gravity condition. Both initial melting and subsequent solidification were included in the simulation. H-based enthalpy-porosity method [50] was used to simulate melting while a model proposed in reference [51] was used to simulate solidification occurring during the LPD growth. A solver was developed in an open-source software OpenFOAM to carry out the simulations. Although the results were found to be in good qualitative agreement with previous numerical and experimental work but some noticeable differences were also observed owing to the absence of convective effects in the present numerical model. The difference was most prominent in the evolution of the growth interface in which faster initial growth interface was predicted along the crucible wall. Since a fixed grid approach was used, so complete growth process could be simulated. The radial and axial crystal composition plots were in line with previous numerical and experimental findings. An attempt was also made to use the developed numerical methodology to simulate earth bound LPD growth including the effects of convection, but accurate results could not be obtained because of the limitations of the solidification model.

Chapter 4

Numerical investigation of the effects of crucible translation in the LPD growth of Si_xGe_{1-x}

4.1 Introduction

In its original form, LPD was developed with the aim of producing uniform composition crystal by maintaining a constant interface temperature during growth [2]. This was accomplished by pulling the crucible during the experiment at a constant rate equal to the growth rate determined empirically. Crucible pulling was commenced after a certain time period from the start of growth. This duration was calculated on the basis of the desired final composition and led to fractional length of graded composition followed by uniform composition crystal. As a further refinement of this work an in situ monitoring system was developed and used to observe and control the temperature of crystal-melt interface [13]. The growth rate was determined by monitoring the interface in the fixed ampoule configuration using this system. It was found that the growth rate varies for an initial length of the grown crystal after which it becomes constant. This observation was then used to decide the initiation of ampoule pulling and the rate at which it is to be pulled out. The interface was detected to be at a fixed position w.r.t ampoule, when the ampoule pulling rate was matched with the growth rate determined previously. A crystal having uniform composition for a length of 5.5 mm was obtained following a initial graded composition corresponding to the time period in which ampoule pulling was not started. However, after the region of uniform composition, wide fluctuations in composition and

poly-crystallization was observed. In continuation of these efforts, a feedback control system was developed to keep the interface at a fixed position with the objective of growing uniform composition crystals [14]. Unlike the previous work in which ampoule was pulled at a constant rate, in this case the pull rate was varied dynamically to keep interface at a fixed position. Two test cases were used to demonstrate the feasibility of growing uniform composition crystals using this feedback control system.

In this chapter, the crucible translation effects on LPD growth configuration are examined both for constant and dynamic pulling rate. The constant pull rate value was chosen to be 0.429 mm/hr based on the experimental results of reference [15]. In the case of dynamic pull rate simulations, the pull rate was varied so as to obtain nearly constant centreline composition.

4.2 Numerical Simulation

As discussed earlier, modeling of the LPD growth process presents a moving boundary problem which calls for the usage of specialized numerical techniques to accurately simulate the transport phenomena associated with this growth method. The moving boundary problem such as solidification can be tackled computationally using fixed and moving grid approaches. It was mentioned before that accurate results could not be obtained using the developed fixed grid numerical solution procedure when convective effects were included because of the limitation of the adopted solidification model. Hence, a moving grid approach was chosen to simulate the translation effects in LPD so as to include the effects of natural convection. In the dynamic grid approach, the mesh is modified after each time step so as to conform the moving and changing boundary.

4.2.1 Choice of the CFD solver

In the previous chapter it was highlighted that using OpenFOAM is particularly useful in situations when a new solution procedure is to be implemented. However, in the present chapter dynamic grid approach was adopted which requires the development of a custom boundary condition for moving the growth interface and a mesh motion strategy but does not require the implementation of any new algorithm unlike the previous chapter. Ansys Fluent is one of most widely used commercial CFD solver and was used to carry out the simulations. Although both OpenFOAM and Ansys Fluent can handle

moving mesh problem but the latter was chosen because of its detailed documentation regarding the implementation of dynamic grid approach, excellent mesh motion tools and the easy to use graphical user interface.

4.2.2 Numerical solution

In comparison to the fixed boundary problem, the field equations include additional terms to account for grid movement which should be computed using the space conservation law [56]. To move the boundary mesh nodes after each time step based on a custom boundary condition along the growth interface, various user-defined functions were developed in Ansys Fluent. The position of the initial growth interface was located by means of an isotherm corresponding to the melting point of germanium. The mesh consists of 4674, 1518, 656, 1002 quadrilateral elements in the melt, seed, source, and quartz regions respectively and the grid size was finalized after performing the mesh independence study. The pressure velocity coupling was handled using the well-known PISO algorithm [57]. A time step of 0.1s was used to carry out the computation. The solution was considered converged when the absolute residuals had fallen below 10^{-4} for the continuity and momentum equations, and 10^{-6} for the energy and mass transport equations. The computational domain, as shown in 2.15, consists of the silicon source at the top, the silicon-germanium melt in the middle, the germanium seed below, and the vertical wall of the quartz ampoule.

4.2.3 Assumptions

In the present numerical simulation model a number of simplifying assumptions were made which may be summarized as follows:

- Local thermodynamic equilibrium is assumed to exist at the dissolution and growth interfaces.
- Silicon-germanium melt is assumed to be a Newtonian and incompressible fluid.
- The melt density change is assumed to be small, and is approximated in the momentum equation by using the well-known Boussinesq approximation in terms of the thermal and solutal expansion coefficients.
- Due to its insignificant effect on the system parameters, the dissolution interface velocity is taken as zero in the simulation: i.e., the dissolution interface is fixed.

- Latent heat of solidification is neglected because of small growth rate.
- Soret and Dufour effects were neglected due to their negligible effect in this system.
- Heat and mass fluxes are given by the well-known Fourier's and Fick's laws, respectively.
- Variation of transport properties with temperature during growth is neglected.
- Mass diffusivity of silicon in the grown crystal is neglected in comparison to its value in the silicon-germanium (initially germanium) melt.
- The growth system is considered axisymmetric, and so are the field equations of the liquid and solid phases.
- The same temperature gradient exists below the initial position of the growth crucible.

4.2.4 Field equations in the presence of moving boundary [58, 59]

The Reynolds transport theorem for an arbitrary deforming control volume is given by:

$$\frac{d}{dt}\int_{CV(t)} \rho\phi dV = \int_{CV(t)} \frac{\partial(\rho\phi)}{\partial t} dV + \oint_{CS(t)} \rho\phi \mathbf{U}_g \cdot d\mathbf{S} \tag{4.1}$$

For material volume with each particle having velocity **U,** the above equation can be written as :

$$\frac{d}{dt}\int_{MV(t)} \rho\phi dV = \int_{MV(t)} \frac{\partial(\rho\phi)}{\partial t} dV + \oint_{MS(t)} \rho\phi \mathbf{U} \cdot d\mathbf{S} \tag{4.2}$$

If the control volume at instant t is chosen in such as way that it exactly coincides with the material volume then the above equation can be modified as :

$$\frac{d}{dt}\int_{MV(t)} \rho\phi dV = \int_{CV(t)} \frac{\partial(\rho\phi)}{\partial t} dV + \oint_{CS(t)} \rho\phi \mathbf{U} \cdot d\mathbf{S} \tag{4.3}$$

Subtracting equation 4.1 from equation 4.3 we get

$$\frac{d}{dt}\int_{MV(t)} \rho\phi dV = \frac{d}{dt}\int_{CV(t)} \rho\phi dV + \oint_{CS(t)} \rho\phi(\mathbf{U} - \mathbf{U}_g) \cdot d\mathbf{S} \tag{4.4}$$

The general balance law for a continuum material can be written as:

$$\frac{d}{dt}\int_{MV(t)} \rho\phi dV = \oint_{MS(t)} \rho\Gamma_\phi(\nabla\phi) \cdot d\mathbf{S} + \int_{MV(t)} S_\phi dV \tag{4.5}$$

Using equation 4.4 and also noting that for time instant t control volume and material volume coincide, the above equation can be simplified as:

$$\frac{d}{dt}\int_{CV(t)} \rho\phi dV + \oint_{CS(t)} \rho\phi(\mathbf{U} - \mathbf{U}_g) \cdot d\mathbf{S} = \oint_{CS(t)} \rho\Gamma_\phi(\nabla\phi) \cdot d\mathbf{S} + \int_{CV(t)} S_\phi dV \tag{4.6}$$

Equation 4.6 represents the general transport equation for an arbitrary control volume having a moving boundary for a scalar transport variable ϕ.

4.2.4.1 Liquid Phase

The field equations for thermo-solutal buoyancy driven flow modeled using the Boussinesq approximation in the melt. As already mentioned before when dealing with dynamic grid approach, an additional term appears in the transport equations to account for mesh motion. The equations are given as follows:

- Continuity

$$\oint_{CS(t)} \rho(\mathbf{n} \cdot \mathbf{U}) dS = 0 \tag{4.7}$$

- Momentum

$$\begin{aligned} \frac{d}{dt}\int_{CV(t)} \rho\mathbf{U} dV + \oint_{CS(t)} \rho[\mathbf{n}.(\mathbf{U} - \mathbf{U_g})]\mathbf{U} dS \; = \; & \oint_{CS(t)} \mu[\mathbf{n} \cdot \nabla\mathbf{U}] dS - \int_{CV(t)} \nabla p dV \\ & - \int_{CV(t)} \rho\mathbf{g}\beta_T(T - T_{ref}) dV \\ & - \int_{CV(t)} \rho\mathbf{g}\beta_C(C - C_{ref}) dV \end{aligned}$$

(4.8)

- Energy

$$\frac{d}{dt}\int_{CV(t)} \rho T dV + \oint_{CS(t)} \rho T[\mathbf{n}\,.\,(\mathbf{U}-\mathbf{U}_g)]dS = \oint_{CS(t)} \rho\alpha[\mathbf{n}\,.\,\nabla T]dS \quad (4.9)$$

- Mass

$$\frac{d}{dt}\int_{CV(t)} \rho C dV + \oint_{CS(t)} \rho C[\mathbf{n}\,.\,(\mathbf{U}-\mathbf{U}_g)]dS = \oint_{CS(t)} \rho D[\mathbf{n}.\nabla C]\,.\,dS \quad (4.10)$$

4.2.4.2 Solid Phase

In the solid phases of the computational domain, the only field equation is the energy balance. In the grown crystal, the energy balance takes the following form:

$$\frac{d}{dt}\int_{CV(t)} \rho T dV - \oint_{CS(t)} \rho T[\mathbf{n}\,.\,\mathbf{U}_g)]dS = \oint_{CS(t)} \rho\alpha[\mathbf{n}\,.\,\nabla T]dS \quad (4.11)$$

For the domains of the quartz wall and silicon solid source, which do not have any moving boundaries, the energy balance is given by:

$$\frac{d}{dt}\int_{CV(t)} \rho T dV = \oint_{CS(t)} \rho\alpha[\mathbf{n}\,.\,\nabla T]dS \quad (4.12)$$

4.2.5 Computational aspects related to moving grid approach

4.2.5.1 Space conservation law [58, 60]

The discretized form of equation 4.6 can be written as:

$$\frac{(\rho_P\phi_P V_P)^n - (\rho_P\phi_P V_P)^{n-1}}{\Delta t} + \sum_f \rho_f(F - F_s)\phi_f = \sum_f (\rho\mathbf{\Gamma})_\mathbf{f}\mathbf{S}_f \bullet (\nabla\phi)_f + S_\phi V_P \quad (4.13)$$

As can be observed from the above equation the grid motion introduces an additional flux term in comparison to the case when the control volume

is not deforming and a temporal derivative term which involves a change in cell volume. The space conservation law provides a relation between these two and can be obtained by setting $\phi = 1$ and considering the density to be constant in equation 4.1

$$\frac{d}{dt}\int_{CV(t)} dV - \int_{CS(t)} d\mathbf{S} \bullet \mathbf{U_g} = 0 \tag{4.14}$$

In the discretized form the above equation reads as :

$$\frac{V_P^n - V_P^{n-1}}{\Delta t} - \sum_f F_s = 0 \tag{4.15}$$

It has been shown in reference [56] that the mesh motion flux should be computed from the space conservation law rather than directly using the grid velocity otherwise a direct usage of grid velocity can result in the introduction of numerical errors (artificial mass sources) which can be avoided by limiting the time-step size, thereby introducing an additional constraint on the maximum time step apart from the temporal accuracy.

4.2.6 Boundary conditions

4.2.6.1 Concentration Field

$$\frac{\partial C}{\partial n} = 0 \tag{4.16}$$

On the dissolution and growth interfaces, local thermodynamic equilibrium was assumed to exist and the liquid equilibrium concentration was prescribed as a function of temperature using the phase diagram of the silicon-germanium system by the following polynomial:

$$C_l^{eq} = a_l \triangle T + b_l \triangle T^2 + c_l \triangle T^3 + d_l \triangle T^4 + e_l \triangle T^5 \tag{4.17}$$

where $\triangle T$ was calculated at the growth interface by $\triangle T = T_{growth} - 938.72$, and at the dissolution interface by $\triangle T = T_{dis} - 938.72$. The coefficients in Eq.(9) were estimated by curve fitting from the silicon-germanium phase diagram for equilibrium (values are given in table 4.1). The solid equilibrium concentration at the growth interface was also estimated similarly by curve fitting the solidus curve in the silicon-germanium phase diagram by using:

Coefficient	a_l	b_l	c_l	d_l	e_l
Value	5.72 x 10^{-2}	1.49 x 10^{-4}	7.48 x 10^{-7}	-1.84 x 10^{-9}	2.21 x 10^{-12}
Coefficient	a_s	b_s	c_s	d_s	e_s
Value	3.82 x 10^{-1}	-6.25 x 10^{-4}	5.95 x 10^{-7}	-2.93 x 10^{-10}	4.45 x 10^{-13}

Table 4.1: Coefficients used to compute equilibrium composition

$$C_s^{eq} = a_s \triangle T + b_s \triangle T^2 + c_s \triangle T^3 + d_s \triangle T^4 + e_s \triangle T^5 \tag{4.18}$$

Initially, the concentration field was set to zero. In order to move the mesh, the grid velocity was computed from the following expression [10]:

$$\rho_s U_g (C_s^{growth,eq} - C_s^{growth,eq}) = \rho_l D_l \frac{\partial C}{\partial n} \tag{4.19}$$

4.2.6.2 Thermal field

At the bottom of ampoule:

$$T = 1146.87 - 4000d \tag{4.20}$$

Along the outer wall of the quartz ampoule adjoining the seed and melt region:

$$T = 1146.87 + 4000(y - d) \tag{4.21}$$

Along the outer wall adjoining the source region, before translation commences:

$$T = 1326.87 \tag{4.22}$$

After translation commences:

$$T = 1146.87 + 4000(y - d) \tag{4.23}$$

$$-\lambda \nabla T = \beta \sigma (T^4 - T_{amb}^4) \tag{4.24}$$

$$T_{amb} = T_{top} - 5 \tag{4.25}$$

The translated distance in the above equations is computed by:

$$d = p\triangle t \tag{4.26}$$

As the latent heat of solidification was neglected due to slow growth, the energy balance at the growth interface leads to the condition of continuous heat flux:

$$\lambda_s \frac{\partial T_s}{\partial n} = \lambda_l \frac{\partial T_l}{\partial n} \tag{4.27}$$

The above condition was also used for all inner boundaries.

4.2.6.3 Flow field

A no-slip boundary condition was used for the flow field along the boundaries of the melt. Initially, the velocities were set to zero.

4.3 Results and Discussion

Numerical simulations were carried out for three cases namely a) stationary, b) at a constant rate of 0.429 mm/h , and c) dynamic translation. The dynamic translation profile was determined to keep the axial silicon composition along the center-line almost constant. The predicted silicon composition from the numerical simulations for all three cases are presented in figures 4.3 and 4.4. First of all, as seen from figures 4.1 and 4.3, for the first two cases (stationary and at a constant translation rate) the numerically predicted axial silicon composition variations agree qualitatively with those of the experiments (the case of zero translation is referred to as baseline in figure 4.1). Similarly, in these two cases, comparison of figures 4.2 and 4.4 shows that the numerically predicted radial silicon composition is also in qualitative agreement with experiments. Figures 4.3 and 4.4 show the numerically predicted axial and radial silicon composition variations under a dynamic translation profile. As seen, the simulation predicts nearly uniform composition both axially and radially. The predicted uniform crystal composition under the dynamic pulling can be attributed to the relatively constant average interface temperature shown in figure 4.5. The dynamic pull rate profile (see figure 4.6) was determined numerically. The simulation was run for small simulation time intervals (around 1 minute) and then the crystal composition

value along the centreline was checked. Depending on whether the composition was tending to increase/decrease/remain constant, the pulling rate was increased/decreased/kept unchanged. The pulling rate values and the corresponding simulation time intervals were recorded and used for obtaining the complete profile. In this way, nearly constant centreline composition and corresponding pulling rate profile were obtained.

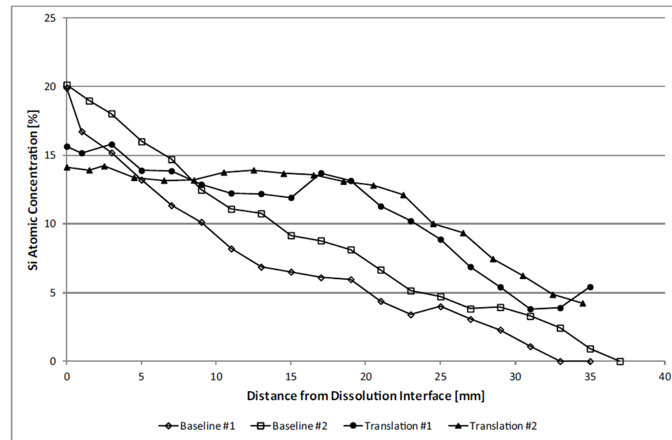

Figure 4.1: Experimental centreline composition profiles of the translated (at 0.429mm/h) and stationary (at 0 mm/h) LPD [15] .

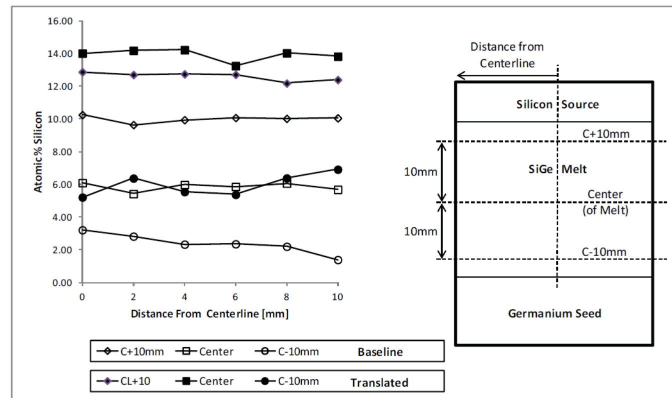

Figure 4.2: Experimental radial composition profiles of the translated (at 0.429mm/h) and stationary (at 0 mm/h) LPD [15]

During the early stages of the growth process, the growth rate is higher thereby requiring higher pulling rates to maintain a constant center-line composition. As the growth proceeds, to achieve a nearly constant composition,

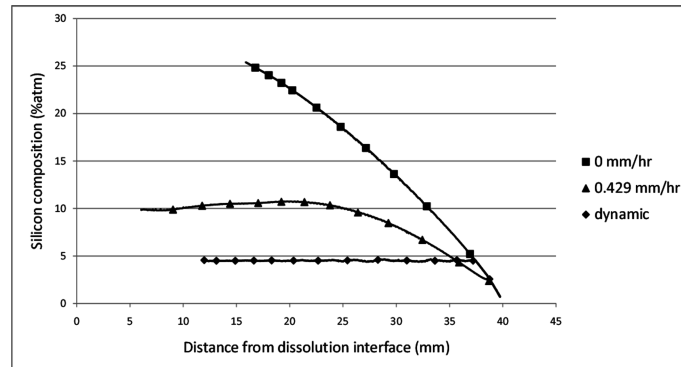

Figure 4.3: Computed axial silicon composition profiles along the centreline of the crystal at a translation rate of 0 mm/hr (stationary), at a constant rate of 0.429 mm/h, and using a dynamic translation (pulling) profile

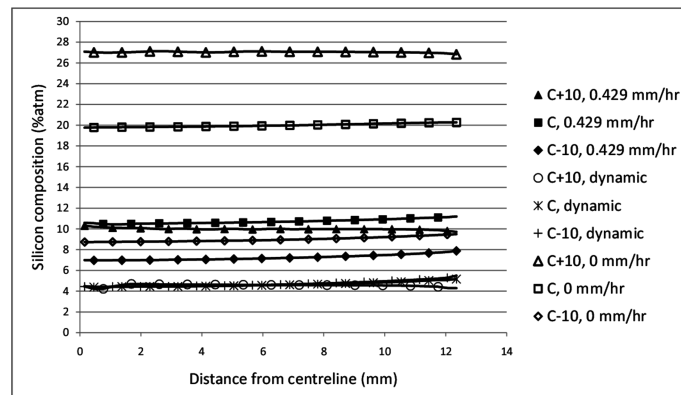

Figure 4.4: Computed radial silicon composition profiles of the crystal at a translation rate of 0 mm/hr (stationary), at a constant rate of 0.429 mm/h, and using a dynamic translation (pulling) profile

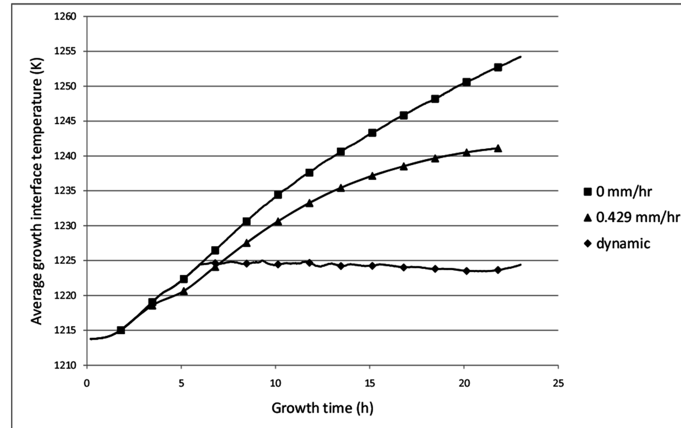

Figure 4.5: Computed average interface temperature at a translation rate of 0 mm/hr (stationary), at a constant rate of 0.429 mm/h, and using a dynamic translation (pulling)profile

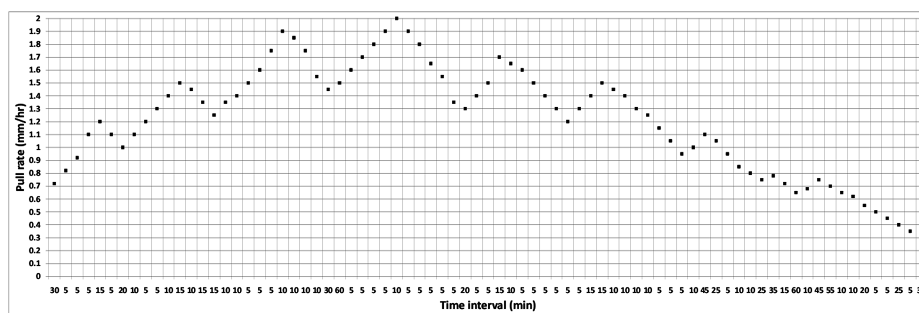

Figure 4.6: Dynamic translation (pulling) profile used in the numerical simulation

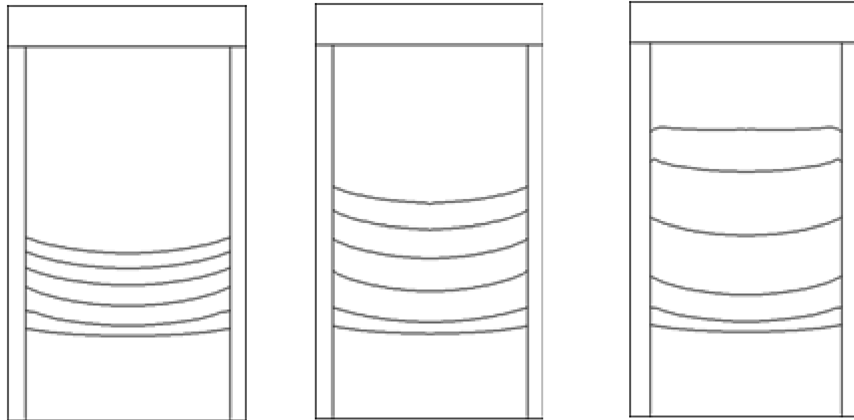

Figure 4.7: Computed interface evolution (contours at 4 hr intervals) for a growth period of 20 hours at the translation rates of a) 0 mm/h, b) 0.429 mm/h, and c) dynamic

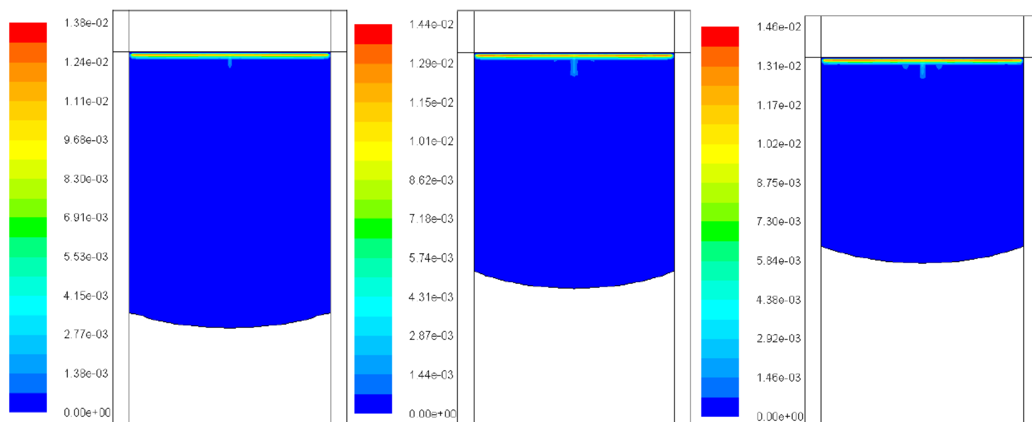

Figure 4.8: Velocity magnitude in the melt after a) 4 hr b) 12 hr, and c) 20 hr of growth time with no translation

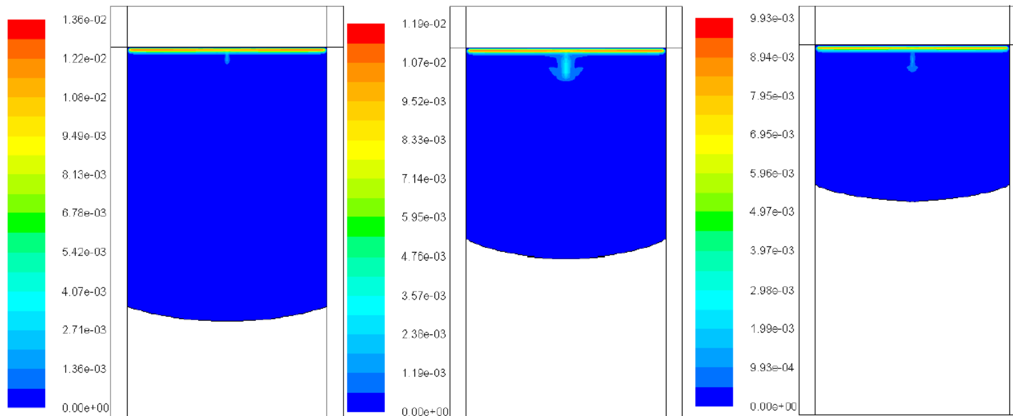

Figure 4.9: Velocity magnitude in the melt after a) 4 hr b) 12 hr, and c) 20 hr of growth time with a translation rate of 0.429 mm/h

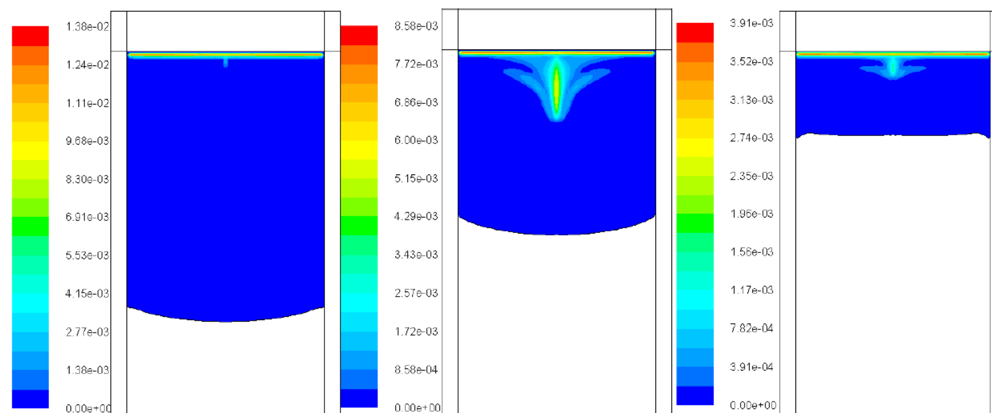

Figure 4.10: Velocity magnitude in the melt after a) 4 hr, b) 12 hr, and c) 20 hr of growth time with dynamic translation

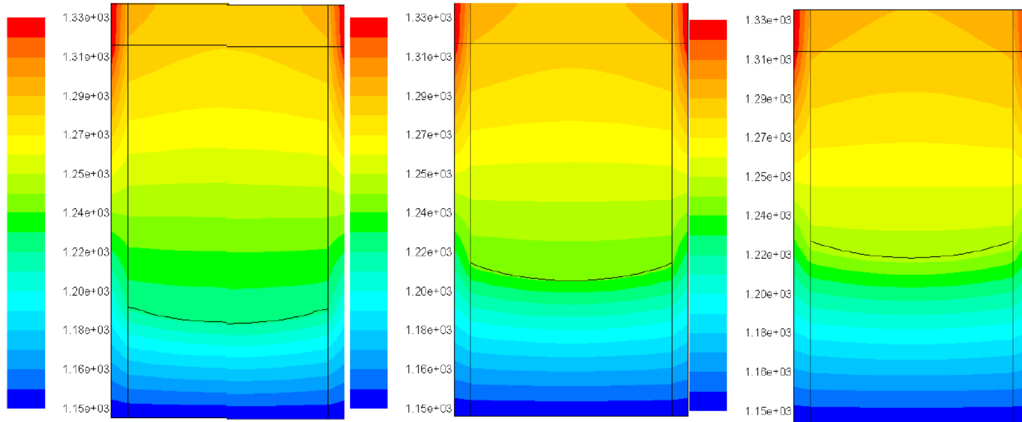

Figure 4.11: Thermal field in the complete domain after a) 4 hr b) 12 hr, and c) 20 hr of growth time with no translation

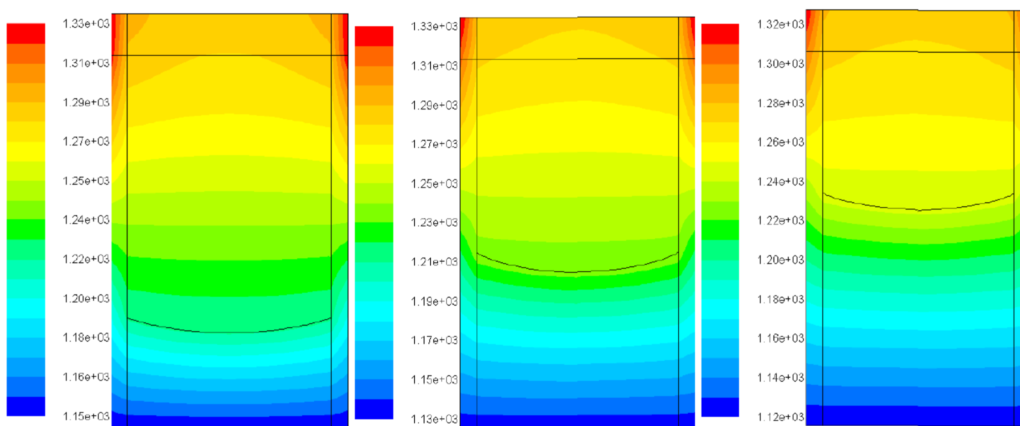

Figure 4.12: Thermal field in the complete domain after a) 4 hr b) 12 hr, and c) 20 hr of growth time with a translation rate of 0.429 mm/h

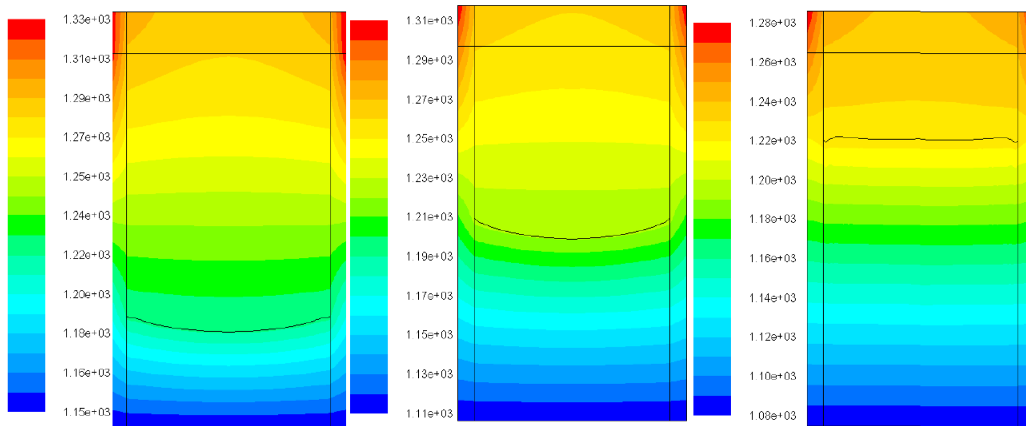

Figure 4.13: Thermal field in the complete domain after a) 4 hr b) 12 hr, and c) 20 hr of growth time with dynamic translation

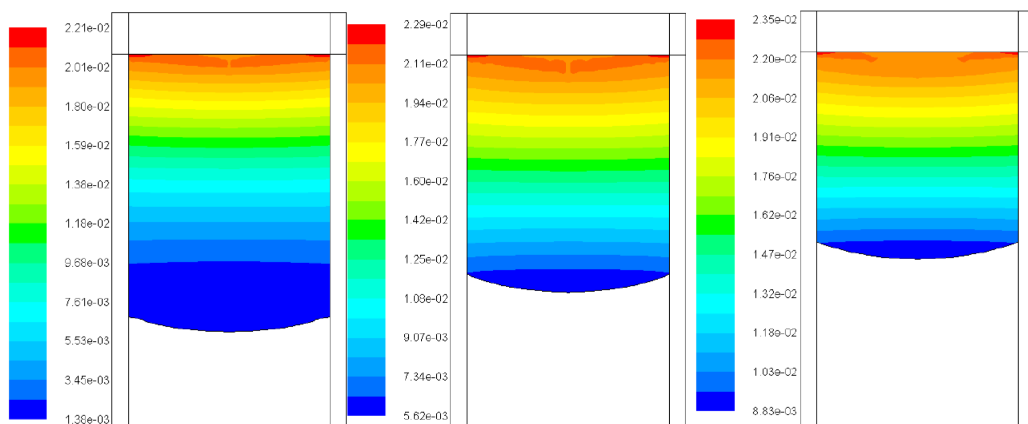

Figure 4.14: Concentration field in the melt after a) 4 hr b) 12 hr, and c) 20 hr of growth time with no translation

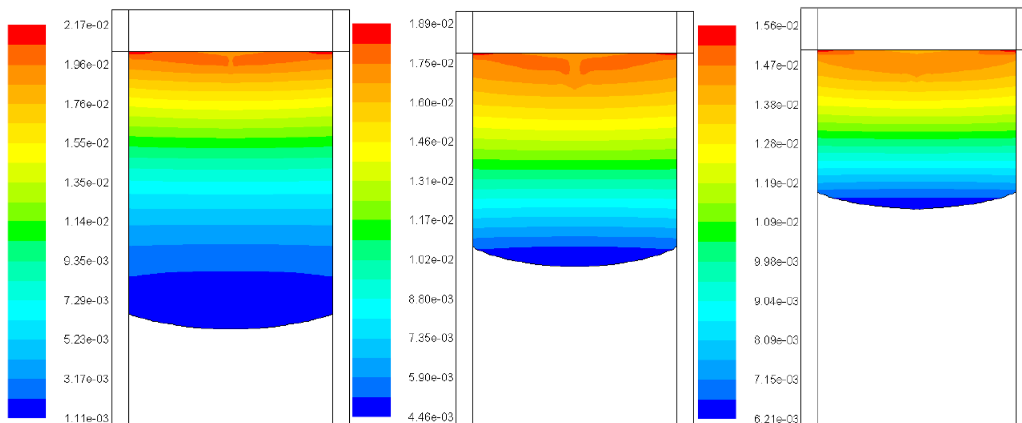

Figure 4.15: Concentration field in the melt after a) 4 hr b) 12 hr, and c) 20 hr of growth time with a translation rate of 0.429 mm/h

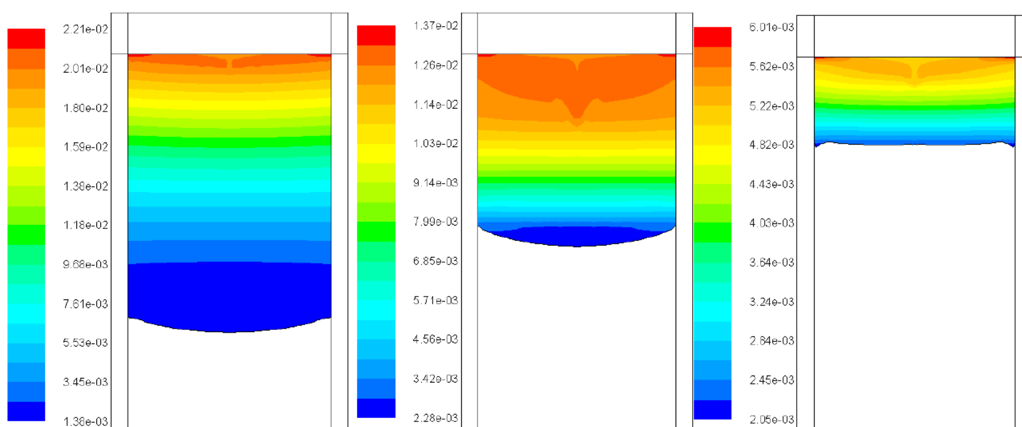

Figure 4.16: Concentration field in the melt after a) 4 hr b) 12 hr, and c) 20 hr of growth time with dynamic translation

much lower pulling rates are needed. As also seen from the computed results presented in figure 4.7, another major advantage of dynamic crucible translation is the significant increase in the growth rate, which leads to faster growth in the given growth time due to the higher pulling rates used . In the stationary LPD growth process (without crucible translation) the solute transport is diffusion dominated except in early stages of growth [10]. As can be seen from figure 4.8, in the later hours of growth, convection is negligible in the entire domain except near the top. This nature of transport practically remains unaltered with crucible translation. This is evident from figures 4.9 and 4.10, which clearly show, the lack of convection near the growth interface for the case of translation with a constant rate and dynamic pulling, respectively. In the case of dynamic pulling, however, the numerical simulation predicts stronger convection (in comparison with the case of stationary and constant translation) with a noticeable increase in the size of the convection cell in the region near the source. This may be attributed to the disturbance in the thermal field caused by the time-dependent pulling rate. However, despite the disturbance in thermal field due to dynamic crucible translation, the presence of stabilizing temperature, concentration and hence density gradients in LPD ensures diffusion continues to remain the dominant mechanism of transport in later hours of growth. This is also reflected in thermal and concentration field distribution (see figures 4.11 to 4.16) which continues to be diffusion dominated despite the introduction of constant and dynamic crucible translation.

4.4 Summary

In this chapter, crucible translation effects in the LPD growth of Si_xGe_{1-x}were investigated numerically. A moving grid approach was adopted so as to include the effects of convection in the numerical model and implementation was carried out in Ansys Fluent. A custom boundary condition was developed to move the growth interface by writing user defined functions in Ansys Fluent. To simulate the crucible translation effects, dynamic temperature boundary condition was prescribed. First, the effect of constant pull rate was examined and compared with the available experimental results and were found to be in good qualitative agreement. Next, the dynamic translation effects were studied by obtaining a dynamic pull profile by running the simulation in small intervals and correcting the pull rate so as to maintain a constant centreline composition. It was shown that it is possible to grow nearly uniform composition crystal by pulling the crucible in a dynamic

fashion. Further, it was also shown that crucible translation has only a very minor impact on transport mechanism of the LPD growth and it continues to be diffusion dominated.

Chapter 5

Numerical simulation of the LPD growth technique subjected to magnetic field

5.1 Static magnetic field

5.1.1 Introduction

The quality of semiconductor crystals can be significantly improved by applying a static magnetic field during the growth process as it helps in minimizing natural convection currents [16, 17]. Natural convection can be effectively suppressed using a static magnetic field in the LPD growth as was shown in the numerical studies [18, 19]. In the experimental work [20, 23], it was found that application of a static magnetic field can slow down the growth rate which in turn was attributed to the suppression of natural convection and a modified thermal field. In order to grow uniform composition with very low silicon content it is necessary to initiate dynamic crucible pulling during early hours of growth. However, it has already been shown in reference [10] that during the early growth hours, convection is quite strong and initiating crucible pulling during this time might not lead to the desired outcome of uniform composition. A static magnetic field can be useful in this situation i.e. when the target silicon composition is quite low and requires early initiation of crucible pulling. This section explores this idea numerically and assesses its effectiveness in producing uniform composition crystal of low silicon content.

5.1.2 Assumptions

Apart from the assumptions listed in section 4.2.3 additional assumptions related to static magnetic field are listed below:

- Vertical magnetic field is aligned with the symmetry axis.
- Contribution of electric potential is neglected as its inclusion has negligible effect [18].
- Effect of static magnetic field on initial melting of germanium is not considered as it is assumed that the static magnetic field is turned on after melting is complete.

5.1.3 Field equations in the presence of static magnetic field

From a numerical simulation point of view, a static magnetic field introduces an additional Lorentz force term in the momentum equation whose computation requires the solution of the electric potential equation apart from the Navier-stokes equations discussed earlier. It has been shown that the contribution of electric potential can be neglected without introducing any significant error [18]. With the above listed assumptions a static magnetic field introduces a radial Lorentz force which can be computed as follows [61] :

$$F_r = -\sigma B^2 v_r \tag{5.1}$$

5.1.4 Results and discussion

Simulations were carried out for two cases a) LPD growth under the action of an applied static magnetic field b) LPD growth under the combined influence of static magnetic field and dynamic translation. A value of 0.4 T was chosen so as to match the value used in the experimental work [20]. As can be seen by comparing figure 5.1 and 5.2, the usage of a static magnetic field completely suppresses convection near the growth interface. It marginally flattens the growth interface especially after 6 hours of growth as can observed from figure 5.3 . In addition, figure 5.3 also shows that the growth rate is not significantly influenced by the application of a static magnetic field. This is in contrast to the experimental observations of reference [20] in which it was found that a static magnetic field considerably reduces the mass transport of silicon due

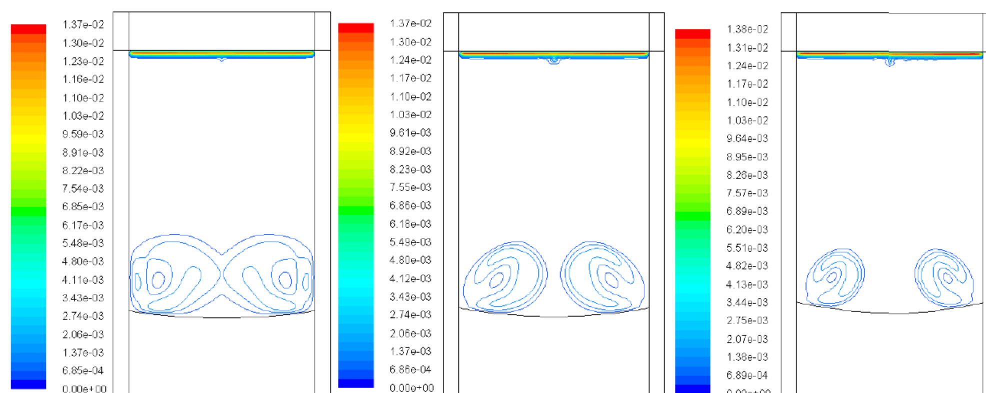

Figure 5.1: Velocity magnitude in the melt after a) 1 hr b) 2 hr, and c) 3 hr of growth time

to the modified thermal field which in turn was attributed to heat loss at top and bottom. As LPD is a diffusion dominated process and suppression of natural convection (which is strong only during early stages of growth) should not slow down the growth rate significantly. A more comprehensive LPD numerical simulation model incorporating furnace heat transfer computation can possibly make a more accurate prediction about this reduction in growth rate. A second important observation in reference [20] was that the extent to which the germanium seed melts under the influence of a static magnetic field was significantly lesser than without the magnetic field. This is most likely due to the suppression of natural convection during the melting of germanium resulting in much lower melt back of the seed. In the present simulations, it was assumed that the static magnetic field is applied after initial melting of germanium is complete and hence the initial growth interface is identical for both cases.

Next, the effects of dynamic translation were examined with early initiation of crucible pulling in order to grow low silicon composition crystal. The usage of a static magnetic field ensures that natural convection is suppressed and early initiation of crucible does not present any problem. Figure 5.4 shows the computed axial composition profile with and without dynamic translation effects. As expected, the case without dynamic translation yields a graded axial composition while dynamic translation results in nearly uniform silicon composition crystal (approximately 1.1 % atomic). A comparison of figures 4.6 and 5.5 indicates that significantly higher pull rates are required to produce low silicon composition crystal. Numerical simulation for the case of dynamic translation could not be continued for the entire

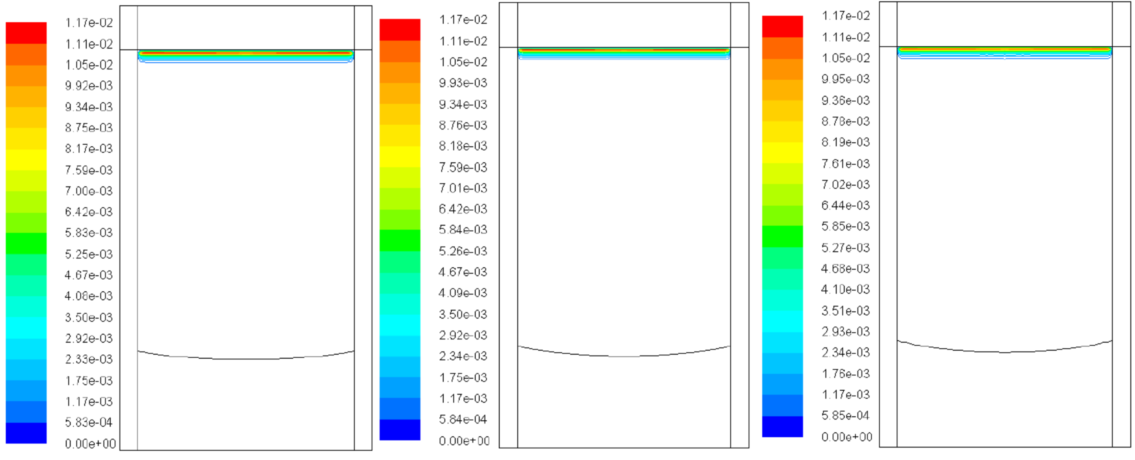

Figure 5.2: Velocity magnitude in the melt after a) 1 hr b) 2 hr, and c) 3 hr of growth time under the action of applied static magnetic field of 0.4 T

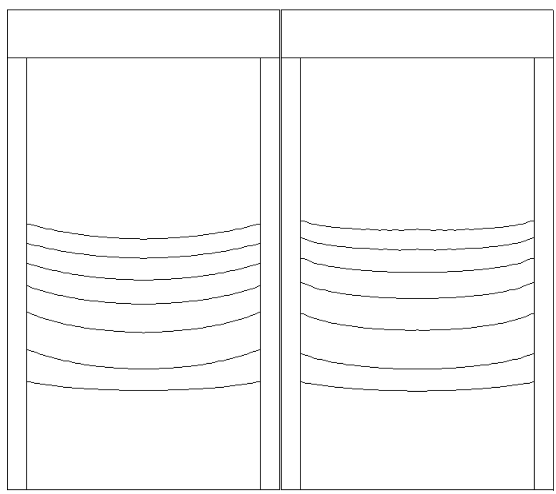

Figure 5.3: Interface evolution for a growth period of 36 hours (6 hour interval) a) without static magnetic field b) with static magnetic field of 0.4 T

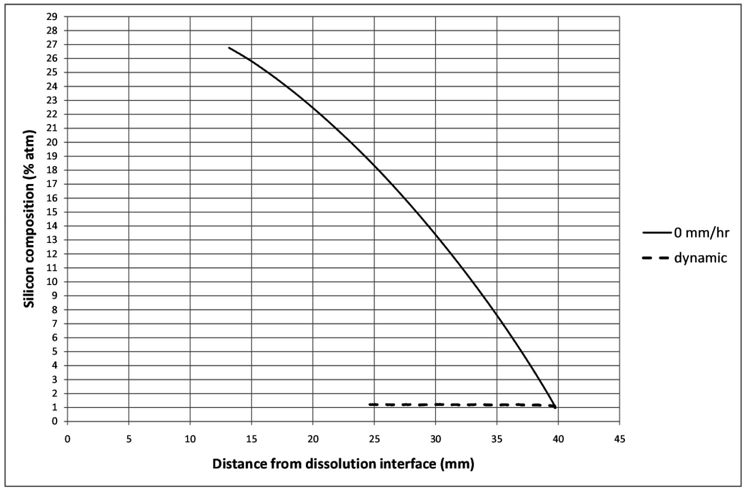

Figure 5.4: Computed axial silicon composition profiles along the centreline of the crystal under the action of applied static magnetic field of 0.4 T at a translation rate of 0 mm/hr (stationary) and using a dynamic translation (pulling) profile

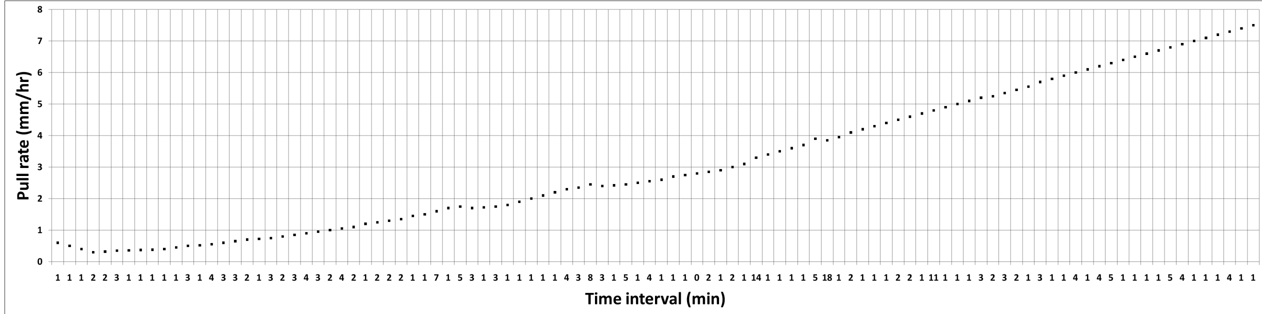

Figure 5.5: Dynamic translation (pulling) profile for producing low silicon composition (1.1 % atm) crystal under the action of applied static magnetic field of 0.4 T

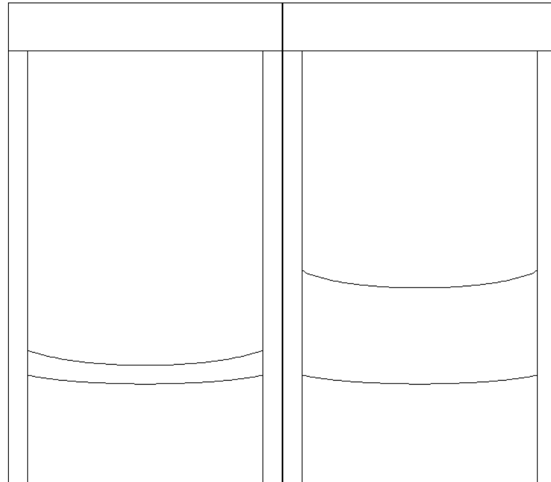

Figure 5.6: Interface displacement after growth period of 5.5 hours and applied static magnetic field of 0.4 T a) without translation b) with dynamic translation

growth period because of mesh quality issues associated with the interface shape which in turn could possibly be attributed to significantly higher pull rates used in this case. Nevertheless, the possibility of growing low composition silicon crystal by initiating early crucible translation was shown by these simulations. Further, a significant improvement in growth rate by employing dynamic translation can be clearly seen from figure 5.6.

5.2 Rotating magnetic field

5.2.1 Introduction

The usage of RMF is quite common in the casting industry to induce melt motion [21]. It is being increasingly used in crystal growth applications as it can improve the quality of grown crystal by making the thermal and concentration field more uniform [22]. It was found in reference [18] that RMF was effective in flattening the growth interface in the LPD growth. Further, in the experimental work [23] it was observed that application of RMF significantly increased the silicon transport. Motivated by the positive numerical and experimental findings related to the application of RMF to the LPD growth this section builds upon the numerical work [18] and simulates the effect of RMF on the LPD technique .

5.2.2 Assumptions

- Local thermodynamic equilibrium is assumed to exist at the dissolution and growth interfaces.
- Silicon-germanium melt is assumed to be a Newtonian and incompressible fluid.
- The melt density change is assumed to be small, and is approximated in the momentum equation by using the well-known Boussinesq approximation in terms of the thermal and solutal expansion coefficients.
- Due to its insignificant effect on the system parameters, the dissolution interface velocity is taken as zero in the simulation: i.e., the dissolution interface is fixed.
- Latent heat of solidification is neglected because of small growth rate.
- Soret and Dufour effects were neglected due to their negligible effect in this system.
- Heat and mass fluxes are given by the well-known Fourier's and Fick's laws, respectively.
- Variation of transport properties with temperature during growth is neglected.
- Mass diffusivity of silicon in the grown crystal is neglected in comparison to its value in the silicon-germanium (initially germanium) melt.
- The flow is considered to be axisymmetric with swirl .
- As the non dimensional frequency K<<1, skin effect is negligible which means that rotating magnetic field distribution remains unaltered in the presence of melt.

5.2.3 Field equations in the presence of rotating magnetic field

From a computational perspective, RMF introduces an additional Lorentz force term in the momentum equations whose computation requires the solution of the electric potential equations apart from the Navier-stokes equations discussed earlier. Under the assumptions listed above the momentum and electric potential equations take the following form [62].

$$\mathbf{B}(r, \varphi, t) = B\left[\hat{r} sin(\varphi - \omega t) + \hat{\varphi} cos(\varphi - \omega t)\right] \tag{5.2}$$

$$
\begin{aligned}
\frac{d}{dt}\int_{CV(t)} \rho \mathbf{U} dV + \oint_{CS(t)} \rho[\mathbf{n.}(\mathbf{U}-\mathbf{U_g})]\mathbf{U} dS \;=\; & \oint_{CS(t)} \mu[\mathbf{n}\,.\,\nabla\mathbf{U}]dS - \int_{CV(t)} \nabla p dV \\
& - \int_{CV(t)} \rho \mathbf{g} \beta_T (T - T_{ref}) dV \\
& - \int_{CV(t)} \rho \mathbf{g} \beta_C (C - C_{ref}) dV + \mathbf{F}^{rot}
\end{aligned}
\tag{5.3}
$$

$$
\overline{F_{\varphi}^{rot}} = 0.5\sigma B(-\frac{\partial \Phi_1}{\partial z} + (\omega r - v_{\varphi})B) \tag{5.4}
$$

$$
\overline{F_{z}^{rot}} = \sigma B(-\frac{1}{2}\frac{1}{r}\frac{\partial (r\Phi_2)}{\partial r} - v_z B) \tag{5.5}
$$

$$
\overline{F_{r}^{rot}} = \frac{\sigma}{2} B(\frac{\partial \Phi_2}{\partial z} - v_r B) \tag{5.6}
$$

$$
-\nabla^2 \Phi_1 + \frac{\Phi_1}{r^2} - B\frac{\partial v_{\varphi}}{\partial z} = 0 \tag{5.7}
$$

$$
-\nabla^2 \Phi_2 + \frac{\Phi_2}{r^2} + B\left(\frac{\partial v_r}{\partial z} - \frac{\partial v_z}{\partial r}\right) = 0 \tag{5.8}
$$

It is imperative to mention an important difference in the momentum equation with and without RMF. In the former case, the field equations are for axisymmetric flow whereas in the latter case the flow is axisymmetric with swirl which essentially means that gradients in the tangential direction are zero but tangential velocity is non zero. It was shown in reference [18] that neglecting the electric potential equations can lead to significant differences in the computation of flow field in comparison to the case when electric potential is taken into account. Hence, in the present research work the computations were performed including the electric potential equations.

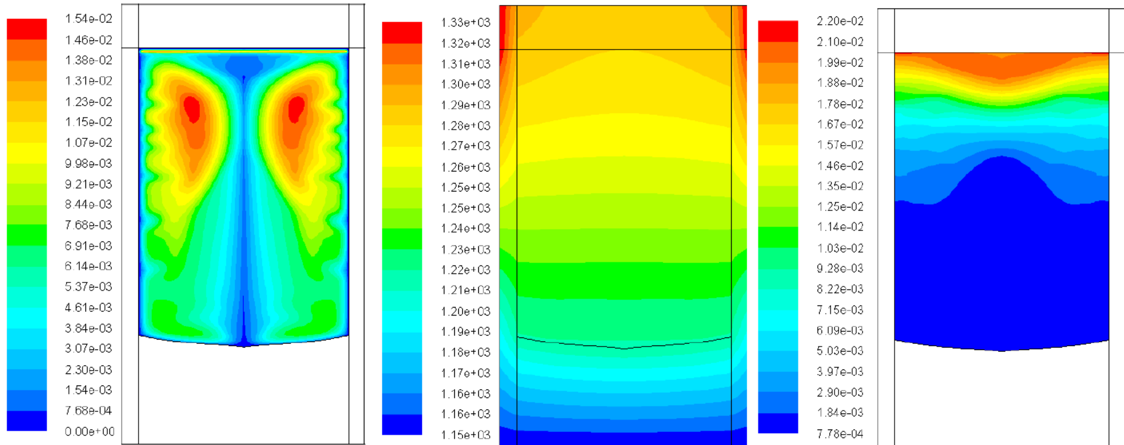

Figure 5.7: Simulation results after 1 hr of growth time in the presence of RMF a) Velocity magnitude b) Temperature field c) Concentration field

5.2.4 Results and discussion

The numerical simulations were carried out for a RMF of 1 mT rotating at 40 Hz which is lower than the value of 5 mT employed in the experimental work [23]. Interface instabilities were observed, possibly due to numerical reasons. RMF induces mixing in the melt and this can be readily observed from figure 5.7 which shows much more uniform distribution of temperature and concentration fields unlike the diffusion dominated distribution observed in LPD without RMF (see figures 4.11 and 4.14). Apart from changing the distribution of field variables, the induced mixing also improves the silicon transport rate significantly as can be seen from 5.8 . However as pointed out earlier due to numerical difficulties complete simulations could not be carried out.

5.3 Summary

This chapter examined the influence of static and rotating magnetic field on the LPD growth numerically. It was shown that static magnetic field can be useful in a situation when a very low silicon composition crystal is required to be grown by the LPD growth. This is because in this situation dynamic crucible pulling should be initiated during early hours of growth when natural convection is quite strong, and it can be effectively suppressed by using static magnetic field. Significantly higher dynamic pull rates were predicted

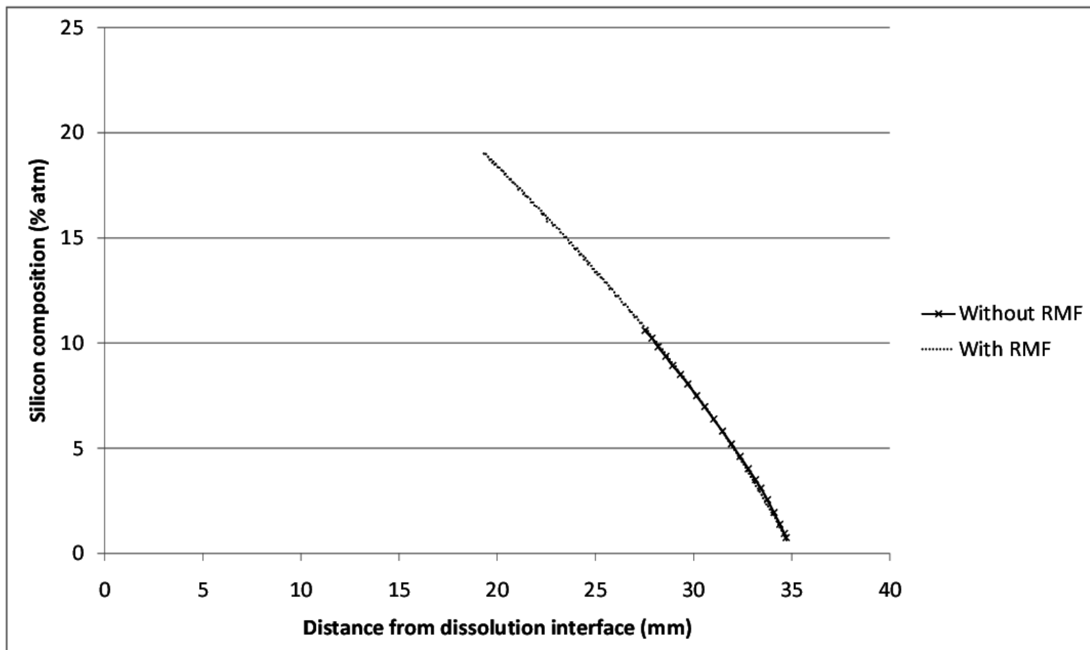

Figure 5.8: Computed axial composition profile with and without RMF

in the simulation than in the previous chapter to grow such low silicon composition crystals and also a substantial improvement in the growth rate was observed. However, complete simulations could not be carried out because of the numerical difficulties. Next, the effect of RMF on the LPD growth system was examined. It was shown that the application of RMF improves the uniformity in the temperature and concentration fields in the melt. Numerical difficulties were encountered in this case as well and simulations could not be completed.

Chapter 6

Conclusion

6.1 Contributions

This dissertation analyzed the LPD growth process using numerical simulation. A fixed grid numerical solver was developed in OpenFOAM to simulate the melting and solidification process. Melt convection was not taken into account as simulation was carried out for zero gravity condition. Results were obtained in the form of interface evolution plot, melt isotherms, and isoconcentration lines, axial and radial composition profiles of the simulated crystal growth and growth velocity plots. These results were compared with the numerical results obtained using a moving grid approach including convective effects and earth based experimental results. Good qualitative agreement was observed with some differences due to the fact that convection was neglected in the developed solver.

- The first major contribution of this work is the development of a novel numerical simulation solver in OpenFOAM based on a fixed grid approach for the LPD growth process. As discussed earlier, this simulation methodology has the following advantages over the moving grid approach:
  - It avoids the need to re-mesh and thus offers a faster and easier way of simulating the LPD process.
  - The mesh quality does not deteriorate with the changing shape of the interface as the interface is represented by the computational cells.
  - As the mesh is fixed, longer simulation times are possible without any mesh quality issues thereby allowing the simulation of the

complete crystal growth process.

In the second part of this thesis, crucible translation effects on LPD growth system were investigated numerically. The effect of both constant and dynamic pull rate was examined with the overall objective of producing uniform composition crystals. A dynamic grid approach was employed so as to include the convective effects and simulation was carried out using Ansys Fluent. Results were presented in the form of velocity, temperature and concentration plots, axial and radial composition profiles of the simulated crystal growth, interface evolution, and average interface temperature plots. In addition, a dynamic pull rate profile was obtained as a part of the simulation process to achieve nearly uniform centreline composition crystal. Numerical results for the constant pull rate were compared with the experimental results and they agreed well qualitatively. Furthermore, nearly uniform centreline crystal composition was predicted with the dynamic pull rate profile. The key contributions of this part of the present study are as follows:

- Investigation of the effect of constant and dynamic pull rate on crystal composition, interface shape, and growth rate.
- Examination of the impact of constant and dynamic translation on the transport phenomena associated with LPD.
- Dynamic pull rate profile to obtain uniform centreline composition.

Next, LPD growth under the influence of static magnetic field was examined. Unlike the experimental findings [20], the numerical simulations did not predict any appreciable reduction in the growth rate due to the static magnetic field. The predominant mechanism of silicon transport in LPD is diffusion [10] and inhibition of natural convection by using a static magnetic field should not alter the transport rate significantly. It indicates that the altered thermal profile [20] due to a static magnetic field is most likely the cause of reduced transport and might require a more comprehensive numerical model incorporating furnace heat transfer computation to predict the reduction in the growth rate. The numerical simulations revealed the effectiveness of static magnetic fields in suppressing natural convection during the early hours of growth which can be exploited in producing uniform composition crystals of low silicon content as it requires early pull initiation. The dynamic crucible translation combined with static magnetic field was used to simulate uniform composition crystal growth (1.1 % atomic silicon). A significant improvement in growth rate was also predicted which should be able to compensate for the experimentally observed reduction in growth rate due to static magnetic field. Another possible alternative is to turn off the static magnetic field after initial growth period (around 4 -5 hours). In

this way, the early initiation of crucible translation can still be carried out in a convection free environment while avoiding the adverse effects of static magnetic field on growth rate.

Finally, the effect of RMF on LPD was explored. It was shown that RMF leads to significant improvement in the growth rate and was in line with the experimental findings [23]. The usage of RMF can significantly reduce the total growth time in LPD to produce graded silicon composition crystals from which the desired composition seed crystals can be obtained. This can be followed by the LPD growth with dynamic translation to produce uniform composition crystals.

6.2 Future work

This research work was numerical in nature and should be followed by some experimental work to validate the numerical findings. Specifically, the results obtained for the LPD growth process under zero gravity condition should be compared with LPD space experiments. On the numerical front, other fixed grid techniques such as level set and phase field method can also be applied to simulate the LPD process and results can be compared with the fixed grid approach employed in this work. In addition, the suitability of using the lattice Boltzmann method to model LPD can also be explored. The dynamic pull rate profiles presented earlier should be utilized to carry out the translation LPD experiments to check its effectiveness in obtaining uniform composition crystals. A series of new dynamic pull rate profiles can be obtained through the numerical simulation procedure discussed in this thesis for various pull initiation times to grow uniform composition crystals of various silicon composition. In this way, a set of dynamic pull rate profiles can be made available to the experimentalist from which an appropriate pull rate profile can be selected depending upon the desired silicon composition. Numerical models can be further refined by carrying out a three dimensional simulation study and incorporating radiative heat transfer to account for furnace heat transfer.

Bibliography

[1] N. Usami. *Silicon-Germanium (SiGe) Nanostructures-Production, Properties and Applications in Electronics*. Edited by Y. Shiraki and N. Usami. Woodhead Publishing, 2011.

[2] K. Nakajima, S. Kodama, S. Miyashita, G. Sazaki, and S.Hiyamizu. Growth of Ge-rich Si_xGe_{1-x} single crystal with uniform composition (x=0.02) on a compositionally graded crystal for use as GaAs solar cells. *Journal of crystal growth*, vol. 205, pp. 270-276, 1999.

[3] M. Yildiz, S. Dost, and B. Lent. Growth of bulk SiGe single crystals by liquid phase diffusion. *Journal of crystal growth*, vol. 280, pp. 151-160, 2005.

[4] V.R. Voller, and C. Prakash. A fixed grid numerical modeling methodology for convection-diffusion mushy region phase-change problems. *International Journal of Heat and Mass Transfer*, vol. 30, pp. 1709-1720, 1987.

[5] H. Ouyang and W. Shyy. Multi-zone simulation of the Bridgman growth process of β-NiAl crystal. *International Journal of Heat and Mass Transfer*, vol. 39(10), pp. 2039-2051, 1996.

[6] H. Ouyang and W. Shyy. Numerical simulation of CdTe vertical Bridgman growth. *Journal of Crystal Growth*, vol. 173, pp. 352-366, 1997.

[7] J. Järvinen, R. Nieminen, and T. Tiihonen. Time dependent simulation of Czochralski silicon crystal growth. *Journal of Crystal Growth*, vol. 180, pp. 468-476, 1997.

[8] D. Morvan, M. El Ganaoui, and P. Bontoux. Numerical simulation of a 2D crystal growth problem in vertical Bridgman-Stockbarger furnace: latent heat effect and crystal-melt interface morphology. *International Journal of Heat and Mass Transfer*, vol. 42, pp. 573-579,1999.

[9] C. Martínez-Tomás and V. Muñoz. CdTe crystal growth process by the Bridgman method: numerical simulation. *Journal of Crystal Growth*, vol. 222, pp. 435-451, 2001.

[10] M. Yildiz and S. Dost. A continuum model for the Liquid Phase Diffusion growth of bulk SiGe single crystals. *International Journal of Engineering Science*, vol. 43, pp. 1059-1080, 2005.

[11] R. Rook and S. Dost. The use of smoothed particle hydrodynamics for simulating crystal growth from solution. *International Journal of Engineering Science,* vol. 45, pp. 75–93, 2007.

[12] R. Rook, M. Yildiz, and S. Dost. Modeling Transient Heat Transfer Using SPH and Implicit Time Integration. *Numerical Heat Transfer, Part B,* vol. 51, pp. 1-23, 2007.

[13] Y. Azuma, N. Usami, T. Ujihara, G. Sazaki, Y. Murakami, S. Miyashita, K. Fujiwara, and K. Nakajima. Growth of SiGe bulk crystal with uniform composition by directly controlling the growth temperature at the crystal–melt interface using in situ monitoring system. *Journal of Crystal Growth*, vol. 224, pp. 204-211, 2001.

[14] Y. Azuma, N. Usami, T. Ujihara, K. Fujiwara, G. Sazaki, Y. Murakami, and K. Nakajima. Growth of SiGe bulk crystals with uniform composition by utilizing feedback control system of the crystal–melt interface position for precise control of the growth temperature. *Journal of Crystal Growth*, vol. 250, pp. 298-304, 2003.

[15] N. Armour. *Transport Phenomena in Liquid Phase Diffusion Growth of Silicon Germanium.* Ph.D thesis, University of Victoria, 2012.

[16] R.W. Series and D.T.J. Hurle. The use of magnetic fields in semiconductor crystal growth. *Journal of Crystal Growth*, vol. 113, pp. 305-328, 1991.

[17] K. Kakimoto and K.W. Yi . Use of magnetic fields in crystal growth from semiconductor melts . *Physica B*, vol. 216, pp. 406 408, 1996.

[18] E. Yildiz , S. Dost, and M. Yildiz. A numerical simulation study for the effect of magnetic fields in liquid phase diffusion growth of SiGe single crystals. *Journal of Crystal Growth*, vol. 291, pp. 497-511, 2006.

[19] E. Yildiz and S. Dost. A numerical simulation study for the combined effect of static and rotating magnetic fields in liquid phase diffusion growth of SiGe. *Journal of Crystal Growth*, vol. 303, pp. 279-283, 2007.

[20] N. Armour and S. Dost. Effect of a static magnetic field on silicon transport in liquid phase diffusion growth of SiGe. *Crystal Research and Technology*, vol. 45(3), pp. 244-248, 2010.

[21] P. A. Davidson. Magnetohydrodynamics in materials processing. *Annual Review of Fluid Mechanics*, vol. 31, pp. 273-300, 1999.

[22] P. Dold, and K.W. Benz. Rotating magnetic fields: fluid flow and crystal growth applications. *Progress in Crystal Growth and Characterization*, vol. 38, pp. 39–58, 1999.

[23] N. Armour and S. Dost. Silicon transport under rotating and combined magnetic fields in liquid phase diffusion growth of SiGe. *Crystal Research and Technology*, vol. 45(4), pp. 335-340, 2010.

[24] W. D. Callister. *Material Science and Engineering, an introduction.* John Wiley & Sons, 2007.

[25] R.W. Olesinski and G. J. Abbaschian. *Bulletin of Alloy Phase Diagrams*, vol. 5, pp. 180-183, 1984.

[26] D.J. Paul. Silicon-Germanium Strained Layer Materials in Microelectronics. *Advanced Materials*, vol. 11(3), pp. 191 204, 1999.

[27] E. Kasper. Prospects of sige heterodevices. *Journal of Crystal Growth*, vol. 150, pp. 921-925, 1995.

[28] J. Konle, H. Presting, H. Kibbel, K. Thonke, and R. Sauer. Enhanced performance of silicon based photodetectors using silicon/germanium nanostructures. *Solid-State Electronics*, vol. 45, pp. 1921–1925, 2001.

[29] K. Said, J. Poortmans, M. Caymax, R. Loo, A. Daami, G. Bremond, O. Kruger, and M. Kittler. High quality, relaxed SiGe epitaxial layers for solar cell application. *Thin Solid Films*, vol. 337(1-2), pp.85–89, 1999.

[30] C. M. Bhandari and D. M. Rowe. Silicon–germanium alloys as high-temperature thermoelectric materials. *Contemporary Physics*, vol. 21(3), pp. 219-242, 1980.

[31] W. G. Pfann. *Zone Melting.* John Wiley & Sons, 1958.

[32] D. Elwell and H.J. Scheel. *Crystal Growth from High Temperature Solutions.* Academic Press, 1975.

[33] S. Dost and B. Lent. *Single Crystal Growth of Semiconductors from Metallic Solutions.* Elsevier, 2006.

[34] N. Armour, S. Dost, and B. Lent. Effect of free surface and gravity on silicon dissolution in germanium melt. *Journal of Crystal Growth*, vol. 299(1), pp. 227–233, 2007.

[35] N. Armour and S. Dost. Diffusion limited silicon dissolution into a germanium melt. *International Symposium on Physical Sciences in Space: Journal of Physics Conference Series*, 327, 2011.

[36] F. Mechighel, N. Armour, S. Dost, and M. Kadja. Mathematical modeling of the dissolution process of silicon into germanium melt. *TWMS Journal of Applied and Engineering Mathematics*, vol. 1(2), pp. 127-149, 2011.

[37] N. Armour and S. Dost. The effect of a static magnetic field on buoyancy-aided silicon dissolution into germanium melt. *Journal of Crystal Growth*, vol. 306, pp. 200– 207, 2007.

[38] N. Armour and S. Dost. Effect of an applied static magnetic field on silicon dissolution into a germanium melt. *Journal of Crystal Growth*, vol. 311(3), pp. 780–782, 2009.

[39] N. Armour and S. Dost. Numerical and experimental study of forced mixing with static magnetic field on sige system. *Fluid Dynamics and Materials Processing*, vol. 5(4), pp. 331–344, 2009.

[40] A. Kidess, N. Armour, and S. Dost. Numerical study of the effect of magnetic fields in dissolution of silicon into germanium melt. *Journal of Crystal Growth*, vol. 312(8), pp. 1402–1406, 2010.

[41] A. Kidess, N. Armour, and S. Dost. A numerical study of silicon dissolution under magnetic fields. *Fluid Dynamics and Materials Processing*, vol. 7(1), pp.29-56, 2011.

[42] OpenFOAM, *OpenFOAM user guide*, 2012.

[43] H.G. Weller, G. Tabor, H. Jasak , and C. Fureby. A tensorial approach to computational continuum mechanics using object-oriented techniques. *Computers in Physics*, vol. 12(6), pp. 620-631, 1998.

[44] H. Jasak. *Error Analysis and Estimation for the Finite Volume Method with Applications to Fluid Flows.* Ph.D thesis, University of London ,1996.

[45] H. Rusche. *Computational Fluid Dynamics of Dispersed Two-Phase Flows at High Phase Fractions*. Ph.D thesis, University of London, 2002.

[46] A. Yeckel and J.J. Derby, *Bulk Crystal Growth of Electronic, Optical and Optoelectronic Materials*, Edited by P. Capper. John Wiley and Sons, 2005.

[47] G. Müller, and J. Friedrich. Challenges in modeling of bulk crystal growth. *Journal of Crystal Growth*, vol. 266, pp. 1-19, 2004.

[48] N. Van den Bogaert, and F. Dupret. Dynamic global simulation of the Czochralski process I. Principles of the method. *Journal of Crystal Growth*. vol. 171, pp. 65-76,1997.

[49] B. Fischer, J. Friedrich, T. Jung, M. Hainke, J. Dagner, T. Fühner, and P. Schwesig. Modeling of industrial bulk crystal growth—state of the art and challenges. *Journal of Crystal Growth*, vol. 275, pp. 240-250, 2005.

[50] W. Shyy, H.S. Udaykumar, M.M. Rao, and R.W. Smith, *Computational Fluid Dynamics with Moving Boundaries*. Taylor & Francis, 1996.

[51] M.F. Zhu , and D.M. Stefanescu. Virtual front tracking model for the quantitative modeling of dendritic growth in solidification of alloys. *Acta Materialia*, vol. 55, pp. 1741-1755, 2007.

[52] G.A. Slack, C. Glassbrenner. Thermal conductivity of germanium from 3°K to 1020°K. *Physical Review*, vol. 120 , pp. 782-789, 1960.

[53] A. Virzi. Computer modelling of heat transfer in Czochralski silicon crystal growth. *Journal of Crystal Growth*, vol. 112, pp. 699-722, 1991.

[54] S. Yesilyurt, L. Vujisic, S. Motakef, F.R. Szofran, and M.P. Volz. A numerical investigation of the effect of thermoelectromagnetic convection (TEMC) on the Bridgman growth of $Ge_{1-x}Si_x$. *Journal of Crystal Growth*, vol. 207, pp. 278–291, 1999.

[55] S.V. Patankar. *Numerical Heat Transfer and Fluid Flow*, Hemisphere, New York, 1980.

[56] I. Demirdžić and M. Perić. Space conservation laws in finite volume calculations of fluid flow. *International Journal. for numerical methods in fluids*, vol. 8, pp. 1037-1050, 1988.

[57] R.I. Issa Solution of the implicitly discretised fluid flow equations by operator-splitting. *Journal of Computational Physics*, vol. 62, pp. 40-65, 1986.

[58] S. Menon. *A numerical study of droplet formation and behaviour using interface tracking methods*. Ph.D. thesis, University of Massachusetts, 2011.

[59] V. Kumar, S. Dost, and F. Durst:. Numerical modeling of crystal growth under strong magnetic fields: An application to the travelling heater method. *Applied Mathematical Modelling*, vol. 31, pp. 589-605, 2007.

[60] H. Jasak and Ž. Tuković. Automatic Mesh Motion for the Unstructured Finite Volume Method. *Trans FAMENA*,vol. 12, pp. 1-20, 2006.

[61] Z. Qin, S. Dost, N. Djilali, and B. Tabarrok. A model for liquid phase electroepitaxy under an external magnetic field II. Application. *Journal of Crystal Growth*, vol. 153, pp. 131-139, 1995.

[62] R.U. Barz, G. Gerbeth, U. Wunderwald, E. Buhrig, and Yu.M. Gelfgat. Modelling of the isothermal melt flow due to rotating magnetic fields in crystal growth. *Journal of Crystal Growth,* vol. 180, pp. 410-421, 1997